



Title	Spin-directed network model for the surface states of weak three-dimensional $Z(2)$ topological insulators
Author(s)	Obuse, Hideaki; Ryu, Shinsei; Furusaki, Akira; Mudry, Christopher
Citation	Physical Review B, 89(15), 155315-1-155315-28 https://doi.org/10.1103/PhysRevB.89.155315
Issue Date	2014-04-21
Doc URL	http://hdl.handle.net/2115/56742
Rights	©2014 American Physical Society
Type	article
File Information	PhysRevB89 155315pdf.pdf



[Instructions for use](#)



Spin-directed network model for the surface states of weak three-dimensional \mathbb{Z}_2 topological insulators

Hideaki Obuse

Department of Applied Physics, Hokkaido University, Sapporo 060-8628, Japan

Shinsei Ryu

Department of Physics, University of Illinois, 1110 West Green St, Urbana, Illinois 61801, USA

Akira Furusaki

*Condensed Matter Theory Laboratory, RIKEN, Wako, Saitama 351-0198, Japan
and RIKEN Center for Emergent Matter Science (CEMS), Wako, Saitama 351-0198, Japan*

Christopher Mudry

*Condensed Matter Theory Group, Paul Scherrer Institute, CH-5232 Villigen PSI, Switzerland
(Received 10 October 2013; revised manuscript received 23 March 2014; published 21 April 2014)*

A two-dimensional spin-directed \mathbb{Z}_2 network model is constructed that describes the combined effects of dimerization and disorder for the surface states of a weak three-dimensional \mathbb{Z}_2 topological insulator. The network model consists of helical edge states of two-dimensional layers of \mathbb{Z}_2 topological insulators which are coupled by time-reversal-symmetric interlayer tunneling. It is argued that, without dimerization of interlayer couplings, the network model has no insulating phase for any disorder strength. However, a sufficiently strong dimerization induces a transition from a metallic phase to an insulating phase. The critical exponent ν for the diverging localization length at metal-insulator transition points is obtained by finite-size scaling analysis of numerical data from simulations of this network model. It is shown that the phase transition belongs to the *two-dimensional symplectic universality class* of Anderson transition.

DOI: [10.1103/PhysRevB.89.155315](https://doi.org/10.1103/PhysRevB.89.155315)

PACS number(s): 73.20.-r, 71.23.-k, 72.15.Rn

I. INTRODUCTION

A strong d -dimensional topological band insulator is a band insulator of noninteracting electrons which is characterized by a nontrivial topological index under certain symmetry constraints. Its $(d-1)$ -dimensional boundary always has gapless boundary states which are extended on the boundary but localized in the direction normal to the boundary. They share, because of the nontrivial topological index, a degree of robustness to perturbations that respect the symmetry constraints.

The simplest example of a strong two-dimensional topological band insulator (without any symmetry constraint) was constructed by Haldane [1]. With periodic boundary conditions, it has two single-particle Bloch bands separated by a gap Δ . Its nontrivial topological invariant is a nonvanishing Chern number that is proportional to the Hall conductivity [2]. This example is a representative of topological band insulators called Chern insulators. In open geometries, Chern insulators support gapless single-particle boundary states, i.e., edge states. These edge states are chiral in that they propagate along the edge either clockwise or anticlockwise depending on the sign taken by the Hall conductivity of the occupied bands. Since intraedge backward scattering is not permitted, these chiral edge states are robust to perturbations [3].

A more intricate example of a strong two-dimensional topological band insulator was constructed by Kane and Mele [4,5]. With periodic boundary conditions, it has four single-particle bands that form two Kramers' pairs of bands as a consequence of time-reversal symmetry. However, spin-rotation symmetry is completely broken by spin-orbit coupling. A gap Δ separates

the two pairs of bands, and the Bloch wave functions of the occupied bands have a nontrivial topological \mathbb{Z}_2 index [5]. In an open geometry, there is a Kramers' pair of edge states, called helical edge states (Fig. 1). This pair is robust to perturbations that respect the time-reversal symmetry [6–8]. This example is a representative of topological band insulators called \mathbb{Z}_2 topological band insulators.

Weak topological band insulators are built out of strong lower-dimensional topological band insulators. For example, a weak three-dimensional topological insulator can be a stack of strong two-dimensional topological insulators as is illustrated in Fig. 2. Weak topological band insulators can support surface states in open geometries that are inherited from the boundary states of their lower-dimensional strong topological band building blocks.

Weak three-dimensional Chern insulators have been studied theoretically in the context of three-dimensional generalizations of the quantum Hall effect [9–16]. Two-dimensional transport at the surface of GaAs/AlGaAs multilayer structures subjected to a large uniform magnetic field parallel to the stacking axis was established in Ref. [17].

Models for weak three-dimensional \mathbb{Z}_2 topological band insulators were constructed simultaneously with models for strong three-dimensional \mathbb{Z}_2 topological insulators [18–21]. Of course, most of the excitement generated by these works was reserved for the strong three-dimensional \mathbb{Z}_2 topological insulators, especially after their experimental discovery in $\text{Bi}_{1-x}\text{Sb}_x$ [22], Bi_2Se_3 [23,24], and TlBiSe_2 [25–28]. A weak three-dimensional \mathbb{Z}_2 topological insulator has been identified experimentally in the form of $\text{Bi}_{14}\text{Rh}_3\text{I}_9$ [29].

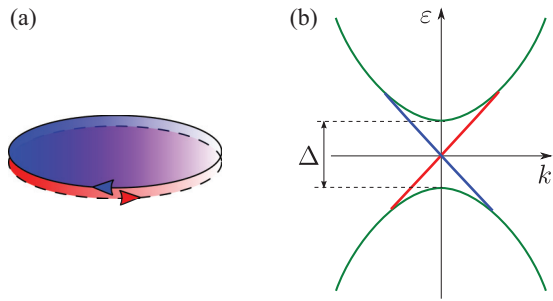


FIG. 1. (Color online) Cartoon representation of a strong two-dimensional \mathbb{Z}_2 topological band insulator with one connected boundary. (a) Electrons are noninteracting and confined within an ellipse in two-dimensional position space. A single pair of counterpropagating helical edge states at zero energy is denoted by the thick and dashed lines with arrows along the connected boundary of the ellipse, respectively. They are confined to this one-dimensional boundary. (b) The single-particle spectrum consists of eigenstates separated by an energy gap Δ and eigenstates crossing the band gap Δ . The former eigenstates are the bulk eigenstates. The latter eigenstates are the edge eigenstates. The momentum k is the momentum along the boundary. The wave functions in position space of bulk eigenstates are supported in the shaded region of the ellipse. The wave functions in position space of edge eigenstates are extended along the edge and labeled by the momentum quantum number k along the edge, while they decay exponentially fast away from the edge.

Two-dimensional surfaces of strong (weak) three-dimensional \mathbb{Z}_2 topological band insulators support an odd (even) number of helical surface states. Each such helical surface state effectively realizes the linear dispersion of a

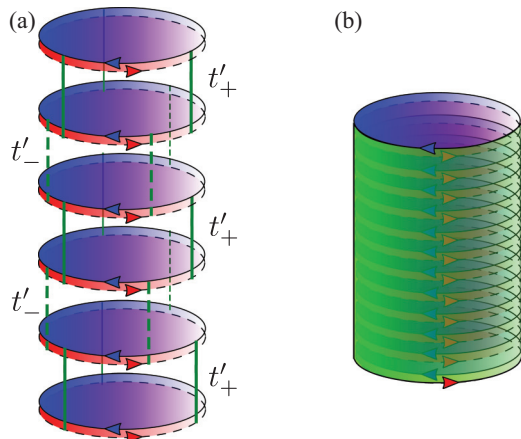


FIG. 2. (Color online) (a) Cartoon representation of a weak layered \mathbb{Z}_2 topological band insulator with open boundary conditions along the layering axis. A vertical line represents the amplitude for the Kramers' degenerate helical edge states of a layer consisting of a strong two-dimensional \mathbb{Z}_2 topological band insulator to hop to one of its adjacent layers. The vertical lines are alternatively drawn with solid and dotted lines in order to indicate that the magnitude of this hopping amplitude takes two distinct values. As a consequence of the breaking of translation invariance by one lattice spacing along the stacking axis, a dimerization gap opens for all helical edge states, i.e., for all surface states of this weak layered \mathbb{Z}_2 topological band insulator. (b) The topology in (a) is that of a cylinder.

massless two-component Dirac particle in two-dimensional momentum space. A single massless two-component Dirac particle can not accommodate a mass term without breaking time-reversal symmetry in two dimensions. In this sense, a single Dirac cone on the surface of a strong three-dimensional \mathbb{Z}_2 topological band insulator is protected by time-reversal symmetry. This is not so for a pair of massless two-component Dirac particles in two dimensions. They can accommodate a mass term that does not break time-reversal symmetry, but breaks some of the lattice symmetries. Thus, a pair of Dirac cones on the surface of a weak \mathbb{Z}_2 topological band insulator is not protected by time-reversal symmetry [18]. For this reason, weak topological band insulators have initially attracted less interest than strong topological band insulators.

In the presence of disorder that preserves the time-reversal symmetry, momentum is not a good quantum number anymore. In fact, the very notion of a spectral gap or of gaplessness is meaningless in the presence of disorder. It is replaced by the notion of mobility edges that defines the windows of single-particle energies for which single-particle states are localized by disorder.

The consequences of disorder weaker than the bulk band gap Δ for the surface states of a strong three-dimensional \mathbb{Z}_2 topological band insulator can be accounted for by describing the helical surface states as massless two-component Dirac fermions in two-dimensional space perturbed by local potentials that break translation invariance along the boundary but preserve time-reversal symmetry. In turn, this effective field theory can be approximated by a nonlinear σ model (NL σ M) with a two-dimensional base space and a target space determined by the symplectic symmetry of the effective Hamiltonian, that is augmented by a topological term [30,31]. This topological term prevents the transition from a conducting to an insulating phase as the disorder strength on the boundary is made arbitrarily large [32], as is implied by the strictly monotonic one-parameter scaling law obeyed by the conductivity σ on a surface of area L^2 that is captured by the beta function $d \ln \sigma / d \ln L$ shown in Fig. 3 [33,34]. By contrast, no topological term augments the NL σ M description of the effect of time-reversal-symmetric disorder for the surface states of a weak three-dimensional \mathbb{Z}_2 topological band insulator [31]. One might be tempted to deduce from this fact that strong disorder always causes localization. This is not so, however.

The even number of Dirac points on the surface of a weak three-dimensional \mathbb{Z}_2 topological band insulator allows a time-reversal-symmetric perturbation, a dimerization, to open a spectral gap $2|m| \ll \Delta$ for the surface states at the cost of breaking some lattice symmetries [18,35]. The effective Dirac Hamiltonian with a dimerization mass m in the clean limit turns out to be the one describing two-dimensional strong \mathbb{Z}_2 topological insulators [35–38]. Hence, the sign of the mass m selects one of the two topologically distinct massive phases of a strong two-dimensional \mathbb{Z}_2 topological band insulator. The surface Dirac points can thus be associated with a quantum critical point separating two massive dimer phases with less lattice symmetries. A defect of the dimerization mass m along a curve on the surface of the weak three-dimensional \mathbb{Z}_2 topological band insulator at which m smoothly changes

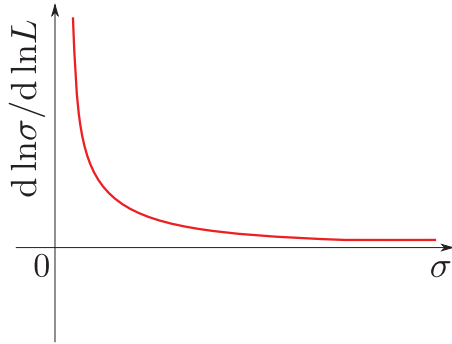


FIG. 3. (Color online) Qualitative beta function $d \ln \sigma / d \ln L$ for the conductivity σ of a massless two-component Dirac fermion on the surface with the area L^2 of a strong three-dimensional \mathbb{Z}_2 topological insulator, when subjected to disorder that preserves time-reversal symmetry. The beta function $d \ln \sigma / d \ln L$ is deduced from the numerics of Refs. [33,34]. It is always positive and the smaller the initial value of the conductivity is the larger the positive value of the beta function.

sign binds a pair of Kramers degenerate helical edge states whose dispersion crosses the gap $2|m|$ of the surface states [35–39]. Provided the disorder is time-reversal symmetric, this quantum critical point has the remarkable property that, perturbed by time-reversal-symmetric surface disorder, it turns into a metallic phase separating two insulating dimerized phases.

This counterintuitive conclusion was first reached by Ringel, Kraus, and Stern for a layered model of a weak three-dimensional \mathbb{Z}_2 topological band insulator based on the sensitivity to twisted boundary condition of spectral flows [40]. Mong, Bardarson, and Moore did a numerical study of the disordered Dirac equation capturing the low-energy and long-wavelength limit of the disordered surface states of a weak three-dimensional \mathbb{Z}_2 topological band insulator that confirmed this prediction and, furthermore, showed that the clean Dirac critical point is smoothly connected to a metallic phase as shown in Fig. 4 [36]. Fu and Kane pointed out the importance of \mathbb{Z}_2 vortices in a description in terms of a NL σ M of disordered surface states of a weak three-dimensional \mathbb{Z}_2 topological band insulator [37]. Furthermore, they have proposed the possibility of a nonmonotonic renormalization-group flow on the line $m = 0$ in Fig. 4. However, the monotonic scaling observed in Ref. [36] seems to indicate that $d \ln \sigma / d \ln L > 0$ at $m = 0$, as is the case of surface states of a strong \mathbb{Z}_2 topological insulator shown in Fig. 3. Finally, a numerical study of the localization properties of a disordered lattice model for a three-dimensional \mathbb{Z}_2 topological band insulator that interpolates from the strong to the weak regimes is consistent with the phase diagram of Fig. 4 [41].

A question that has been left open so far is that of the nature of the phase transition between the insulating and the metallic phases in Fig. 4. In this paper, we construct a two-dimensional network model for the surface states of a weak three-dimensional \mathbb{Z}_2 topological band insulator. We call this network model the two-dimensional spin-directed \mathbb{Z}_2 network model. It differs from a two-dimensional \mathbb{Z}_2

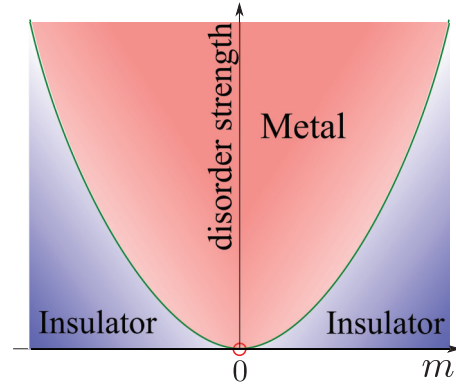


FIG. 4. (Color online) Phase diagram from Ref. [36] for the surface states of a weak three-dimensional \mathbb{Z}_2 topological band insulator as a function of the mass that opens a band gap at the Dirac points (horizontal axis) and the disorder strength (vertical axis). It is assumed that the disorder does not mix surface states localized on disconnected boundaries of the three-dimensional \mathbb{Z}_2 topological band insulator [32]. The origin of the phase diagram is the critical point corresponding to an even number of two-component massless Dirac fermions at their Dirac point.

network model that we constructed in Ref. [42] to study the effects of disorder on the phase diagram of a strong two-dimensional \mathbb{Z}_2 topological band insulator [43,44]. For the two-dimensional spin-directed \mathbb{Z}_2 network model, we argue by considering several limiting cases and by mapping it to effective Dirac Hamiltonians that, without dimerization, there is no insulating phase even when disorder is strong. With a finite dimerization, we establish numerically the existence of three phases, two insulating phases that are separated by a metallic phase. We show that, aside from being continuous, the quantum phase transition between the insulating and metallic phases belongs to the two-dimensional universality class with symplectic symmetry within the theory of Anderson localization, irrespectively of whether the insulating phases are topologically trivial or nontrivial.

The paper is organized as follows. The two-dimensional spin-directed \mathbb{Z}_2 network model that describes the combined effects of dimerization and disorder for the surface states of a weak three-dimensional \mathbb{Z}_2 band insulator is constructed in Sec. II. This model is studied in Sec. III, in which the main numerical results of this paper are explained. A generalization of the spin-directed \mathbb{Z}_2 network model to incorporate surface states of an odd stacking number of strong \mathbb{Z}_2 topological insulators is presented in Sec. IV. Section V is devoted to the two-dimensional spin-directed \mathbb{Z}_2 network model that describes the combined effects of trimerization and disorder on the surface states of a weak three-dimensional \mathbb{Z}_2 band insulator. Section VI closes the paper by summarizing our results. We also present in Appendices A and B the relationship between the model from Sec. II A captured by Fig. 2, the two-dimensional spin-directed \mathbb{Z}_2 network model from Sec. II B, and two-dimensional Dirac fermions [45]. Thereby, we establish the complementarity of our results to those from Ref. [36]. The parameter sets used in our finite-size scaling analysis are given in Appendix C.

II. DEFINITIONS AND MAIN RESULTS

A. Quasi-one-dimensional model for the surface states of a weak three-dimensional \mathbb{Z}_2 topological insulator

We start from the model of a weak three-dimensional \mathbb{Z}_2 topological band insulator that is depicted in Fig. 2. It consists of a stacking of layers, each of which represents a strong two-dimensional \mathbb{Z}_2 topological band insulator depicted in Fig. 1(a). We assume that all pancakes in Fig. 2(a) are identical. The single-particle spectrum corresponding to any pancake in Fig. 2(a) is shown in Fig. 1(b). It consists of two continua corresponding to bulk single-particle eigenstates separated by the band gap Δ and of a pair of Kramers' degenerate helical edge states crossing the bulk gap. We will always assume that Δ is much larger than the amplitude $\max\{|t'_-|, |t'_+|\}$ for edge states on adjacent pancakes to hop between layers. Here, t'_+ is depicted by a solid line in Fig. 2, while t'_- is drawn as a dotted line in Fig. 2. The characteristic energy

$$\delta' := +\sqrt{\frac{|t'_+|^2 - t_-^2}{2}} \quad (2.1a)$$

quantifies the amount by which translation symmetry by one stacking layer is broken, i.e., the amount of dimerization about the average hopping amplitude

$$t' := +\sqrt{\frac{t'_+^2 + t_-^2}{2}}. \quad (2.1b)$$

The hierarchy of energy scales

$$\Delta \gg t' \gg \delta' \quad (2.1c)$$

will be assumed.

Assumption (2.1c) justifies ignoring the degrees of freedom from the bulk altogether and keeping only the degrees of freedom living on the edges of Fig. 2 for energies below Δ . In Appendix A, we present a quasi-one-dimensional Hamiltonian that governs the dynamics of the surface states of Fig. 2 when

$$\Delta \gg t' \gg \delta'. \quad (2.2)$$

This approach is inspired from similar constructions when time-reversal symmetry is broken (see Refs. [46–49]). We show in Appendix A that there exists a continuum limit along the stacking axis that reduces this effective Hamiltonian to the Dirac Hamiltonian studied numerically by Mong, Bardarson, and Moore in Ref. [36].

B. Two-dimensional spin-directed \mathbb{Z}_2 network model for the surface states of a weak three-dimensional \mathbb{Z}_2 topological insulator

Alternatively, we may encode the dynamics of the surface states of Fig. 2, under the assumption that the hierarchy of energy scales (2.1c) holds, in terms of the unitary scattering matrix of a two-dimensional spin-directed \mathbb{Z}_2 network model.

The elementary building block of the two-dimensional spin-directed \mathbb{Z}_2 network model is a 4×4 unitary matrix S that scatters four incoming plane waves into four outgoing plane waves. The conventions on the labels of the scattering states that we choose to represent S are defined in Fig. 5. If we demand that this 4×4 unitary matrix S preserves

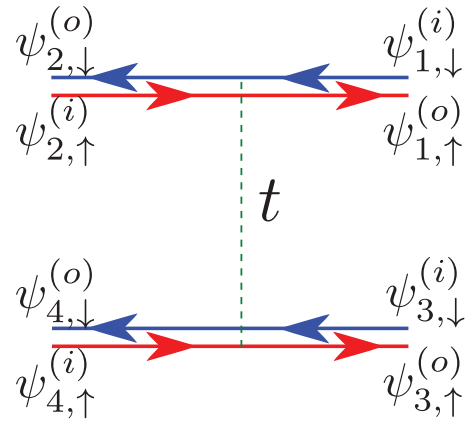


FIG. 5. (Color online) An elementary scattering event in the spin-directed \mathbb{Z}_2 network model maps four incoming plane waves into four outgoing plane waves through a unitary 4×4 matrix S compatible with the operation of time reversal. By demanding that the operation of time reversal is an antiunitary operation that squares to minus the 4×4 identity matrix, the scattering matrix S can break spin-rotation symmetry (hence the spin labels on the plane waves), but preserves time-reversal symmetry. In other words, the scattering matrix belongs to the symplectic class of scattering matrices. The matrix S is represented by Eq. (2.3).

time-reversal symmetry, whereby time reversal is represented by an antiunitary map on scattering states that squares to minus the 4×4 unit matrix, we obtain the representation

$$\begin{pmatrix} \psi_{1,\uparrow}^{(o)} \\ \psi_{2,\downarrow}^{(o)} \\ \psi_{3,\uparrow}^{(o)} \\ \psi_{4,\downarrow}^{(o)} \end{pmatrix} = S \begin{pmatrix} \psi_{2,\uparrow}^{(i)} \\ \psi_{1,\downarrow}^{(i)} \\ \psi_{4,\uparrow}^{(i)} \\ \psi_{3,\downarrow}^{(i)} \end{pmatrix}, \quad (2.3a)$$

where the scattering matrix that maps four incoming into four outgoing plane waves has the 2×2 block structure

$$S := e^{+i\phi_0} \begin{pmatrix} r e^{+i\phi_3} \sigma_0 & t Q \\ -t Q^\dagger & r e^{-i\phi_3} \sigma_0 \end{pmatrix}. \quad (2.3b)$$

The real numbers r and t obey the condition

$$1 = r^2 + t^2 \iff r = \tanh x, \quad t = \frac{1}{\cosh x}, \quad x \in \mathbb{R}, \quad (2.3c)$$

and may be interpreted as the reflection and transmission amplitudes, respectively, upon inspection of the transformation laws of the labels 1 and 2 on the one hand and 3 and 4 on the other hand from Fig. 5. The 2×2 matrix Q is defined by

$$\begin{aligned} Q &= \begin{pmatrix} e^{+i\phi_1} \cos \theta & e^{+i\phi_2} \sin \theta \\ e^{-i\phi_2} \sin \theta & -e^{-i\phi_1} \cos \theta \end{pmatrix} \\ &= i \sin \phi_1 \cos \theta \sigma_0 + \cos \phi_2 \sin \theta \sigma_1 \\ &\quad - \sin \phi_2 \sin \theta \sigma_2 + \cos \phi_1 \cos \theta \sigma_3. \end{aligned} \quad (2.3d)$$

It acts on the spin-up and -down labels of the incoming and outgoing plane waves through the unit 2×2 matrix σ_0 and the three Pauli matrices σ_1 , σ_2 , and σ_3 . The parameter $0 \leq \theta \leq \pi/2$ quantifies the amount of spin-rotation symmetry breaking. When $\theta = 0$, the $SU(2)$ spin-rotation symmetry is

broken down to the subgroup $U(1)$. Any $0 < \theta \leq \pi/2$ breaks the residual $U(1)$ symmetry by a spin-flip process. The rate of this spin-flip tunneling is maximal for $\theta = \pi/2$. The remaining four phases ϕ_j ($0 \leq \phi_j < 2\pi$, $j = 0, 1, 2, 3$) parametrize the phase arbitrariness of incoming and outgoing plane waves compatible with the condition

$$\begin{pmatrix} \sigma_2 & 0 \\ 0 & \sigma_2 \end{pmatrix} S^* \begin{pmatrix} \sigma_2 & 0 \\ 0 & \sigma_2 \end{pmatrix} = S^\dagger \quad (2.3e)$$

that implements time-reversal symmetry on the scattering matrix. The sign of the amplitudes t and r can always be absorbed into the shifts $\phi_{1,2} \rightarrow \phi_{1,2} + \pi$ and $\phi_3 \rightarrow \phi_3 + \pi$, respectively. Hence, we may assume without loss of generality that t and r are positive numbers.

A two-dimensional spin-directed \mathbb{Z}_2 network model is defined by arranging a collection of elementary scattering events, with possibly distinct values for the parameters t , θ , ϕ_j ($j = 0, 1, 2, 3$), as is shown in Fig. 6. These network models are spin directed because, if all transmission amplitudes are chosen to vanish, there is no flipping of the spin quantum numbers so that there are M independent pairs of Kramer's degenerate helical edge states propagating unimpeded along M one-dimensional channels.

The two-dimensional spin-directed \mathbb{Z}_2 network model is thus different from the two-dimensional (undirected) \mathbb{Z}_2 network model that realizes strong two-dimensional \mathbb{Z}_2 topological insulators studied in Refs. [42–44], as can be verified by comparing Figs. 6 to 7. In the two-dimensional (undirected) \mathbb{Z}_2 network model, the nodes labeled by r in Fig. 7 are obtained from those labeled by t through a 90° rotation. Hence, the two-dimensional (undirected) \mathbb{Z}_2 network model is invariant (on average) under 90° rotation, whereas there is no discrete rotation symmetry for the two-dimensional spin-directed \mathbb{Z}_2 network model.

Disorder is introduced in any two-dimensional spin-directed \mathbb{Z}_2 network model by choosing the four phases ϕ_j ($j = 0, 1, 2, 3$) of any elementary scattering process making up a network model to be random numbers independently and identically distributed with a uniform distribution on the interval

$$\left[-\frac{\delta\phi}{2}, +\frac{\delta\phi}{2} \right]. \quad (2.4)$$

In this paper, we study the combined effects of dimerization and disorder on the two-dimensional spin-directed \mathbb{Z}_2 network model. To incorporate dimerization, we assume that the squared amplitude of the transmission (reflection) amplitude alternates in a periodic fashion between the two values labeled by \pm of

$$0 \leq t_\pm^2 \leq 1 \quad (r_\pm^2 = 1 - t_\pm^2), \quad (2.5a)$$

where

$$t_\pm^2 := \begin{cases} t^2 \pm \delta^2, & \text{if } t_+^2 > t_-^2 \\ t^2 \mp \delta^2, & \text{if } t_+^2 < t_-^2. \end{cases} \quad (2.5b)$$

Equation (2.5b) emphasizes that the choice of which of the squared transmission amplitudes t_+^2 and t_-^2 is the largest is arbitrary for an alternating covering of the network. When $\delta = 0$, there is no dimerization. Parameter space Ω_{4d} for

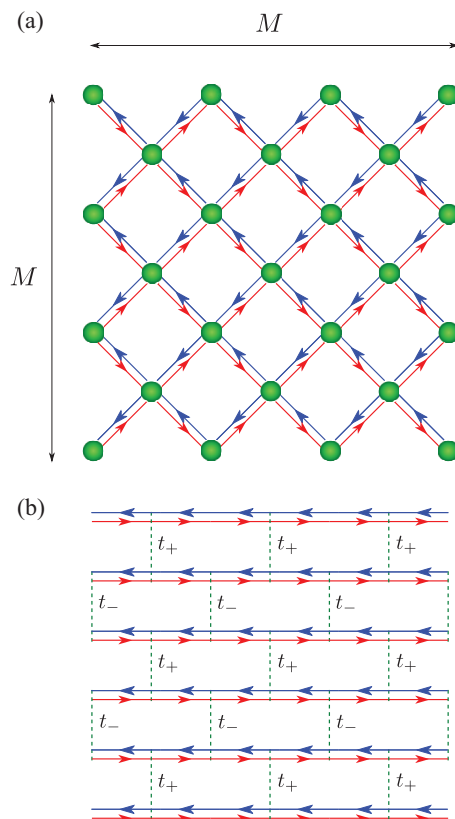


FIG. 6. (Color online) A two-dimensional spin-directed \mathbb{Z}_2 network model built out of the elementary scattering processes shown in Fig. 5 in the vertex (a) and the brick-wall representations (b), respectively. The red and blue lines represent the flow of electrons with up and down spins, respectively. The dimensions of both networks in (a) and (b) are $M \times M$ with $M = 6$. In both representations, one M counts the number of pairs of up and down spins that move from left to right or right to left, while the other M counts the number of pairs of up and down spins that move from up to down or down to up. In the brick-wall representation, each dotted line represents an elementary scattering shown in Fig. 5 with the transmission amplitude t_+ or t_- . This periodic pattern implements one of two dimerization patterns, the other one following from interchanging t_+ and t_- .

the two-dimensional spin-directed \mathbb{Z}_2 network model with disorder and dimerization is four dimensional. We choose the parametrization

$$\Omega_{4d} = \Omega_{4d}^+ \cup \Omega_{4d}^- \quad (2.6a)$$

with

$$\begin{aligned} \Omega_{4d}^\pm := \{ & (t^2, \theta, \delta\phi, \pm\delta^2) | t^2 \in [0, 1], \quad \theta \in [0, \pi/2], \\ & \delta\phi \in [0, 2\pi[, \delta^2 \in [0, 1], \quad 0 \leq t^2 + \delta^2 \leq 1 \}. \end{aligned} \quad (2.6b)$$

However, in most cases, we will choose the disorder to be maximal in that

$$\delta\phi = 2\pi, \quad (2.7a)$$

the exception being Sec. III G where we study the dependence of the normalized localization length on $\delta\phi$. If so, parameter

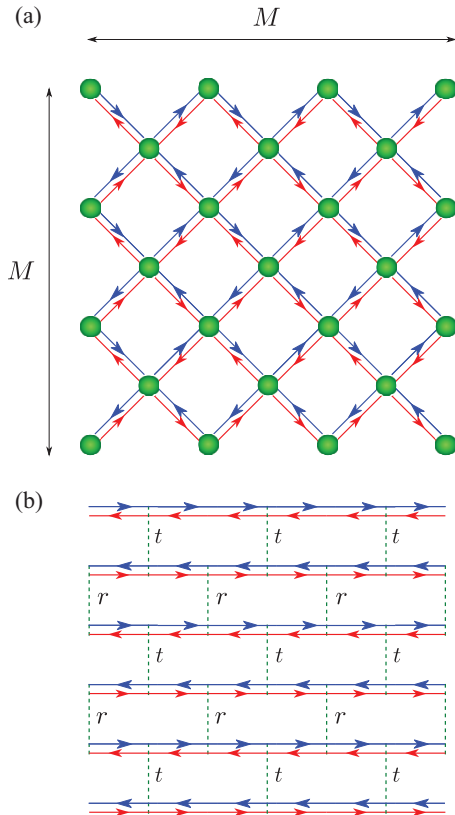


FIG. 7. (Color online) The two-dimensional \mathbb{Z}_2 network model studied in Refs. [42–44] for a strong two-dimensional \mathbb{Z}_2 topological insulator with $M = 6$ in the vertex (a) and the brick-wall representations (b), respectively. Note that the flow direction of the same spin component (up or down) is opposite on adjacent layers in (b), in contrast to Fig. 6(b).

space is three dimensional and given by

$$\Omega_{3d} = \Omega_{3d}^+ \cup \Omega_{3d}^- \quad (2.7b)$$

with

$$\begin{aligned} \Omega_{3d}^\pm := \{ & (t^2, \theta, \pm\delta^2) | t^2 \in [0, 1], \theta \in [0, \pi/2], \\ & \delta^2 \in [0, 1], 0 \leq t^2 + \delta^2 \leq 1 \}. \end{aligned} \quad (2.7c)$$

The interchange of t_+^2 and t_-^2 amounts to the interchange of Ω_{3d}^+ and Ω_{3d}^- (here either $x = 4$ or 3).

We show in Appendix B that there exist two continuum limits of the two-dimensional spin-directed \mathbb{Z}_2 network model in the vicinity, as measured by a small δ^2 , of the lines $\theta = \pi/2$ with t^2 arbitrary and $\theta = 0$ with t^2 arbitrary, respectively. The line with $\theta = \pi/2$ delivers the Dirac Hamiltonian studied numerically by Mong, Bardarson, and Moore in Ref. [36].

C. Some limiting cases without dimerization

There are several lines in the two-dimensional subspace

$$(t^2, \theta, \delta^2 = 0) \in [0, 1] \times [0, \pi/2] \quad (2.8)$$

of the parameter space (2.7) without dimerization for which the two-dimensional spin-directed \mathbb{Z}_2 network model simplifies.

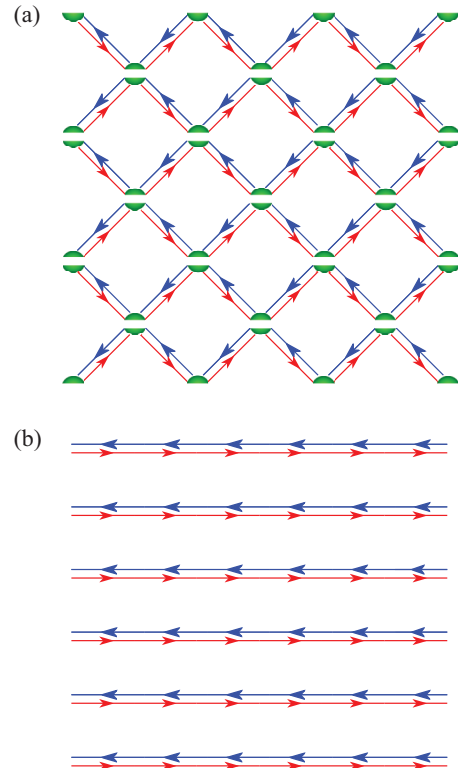


FIG. 8. (Color online) When $\delta^2 = t^2 = 0$, the two-dimensional spin-directed \mathbb{Z}_2 network model from Fig. 6 decouples into M one-dimensional channels, each of which consists of a single Kramers' degenerate pair of helical edge states that propagate unimpeded by the disorder. Panels (a) and (b) are drawn using the vertex and the brick-wall representations, respectively.

1. Limit $t^2 = 0$ without dimerization

We set

$$\delta^2 = t^2 = 0. \quad (2.9)$$

When $t^2 = 0$, the elementary scattering matrix from Eq. (2.3) is block diagonal and independent of θ ,

$$S = e^{+i\phi_0} \begin{pmatrix} e^{+i\phi_3} \sigma_0 & 0 \\ 0 & e^{-i\phi_3} \sigma_0 \end{pmatrix}. \quad (2.10)$$

The two-dimensional spin-directed \mathbb{Z}_2 model of Fig. 6 is shown in Fig. 8 when $\delta^2 = t^2 = 0$. It represents M decoupled one-dimensional channels, each of which consists of a Kramers' degenerate pair of helical edge states that propagates unimpeded by the disorder. The localization length is infinite in the direction of propagation of these helical edge states, while it is vanishing in the orthogonal direction. The fixed point (2.9) is thus the *quasi-one-dimensional symplectic metallic fixed point*.

2. Limit $\theta = 0$ without dimerization

We set

$$\delta^2 = \theta = 0. \quad (2.11)$$

Since θ measures in dimensionless units the characteristic strength of spin-orbit interactions with the convention that

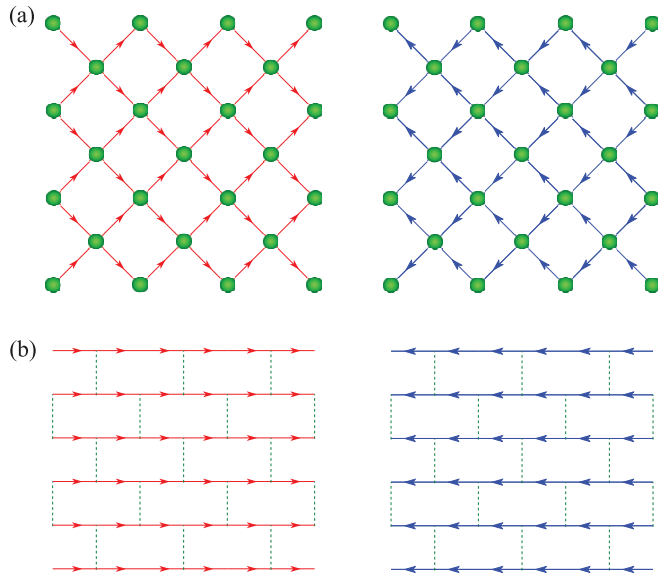


FIG. 9. (Color online) When $\delta^2 = \theta = 0$, the two-dimensional spin-directed \mathbb{Z}_2 network model from Fig. 6 decouples into two directed CC models that are related by time reversal. Panels (a) and (b) are drawn using the vertex and the brick-wall representations, respectively.

the Rashba-like spin-orbit coupling vanishes when $\theta = 0$, the spin-directed \mathbb{Z}_2 network model with $\delta^2 = \theta = 0$ is expected to decouple into two two-dimensional directed Chalker-Coddington (CC) models [10], one for the spin-up and one for the spin-down plane waves, that are related by time-reversal symmetry. This decoupling is shown in Fig. 9. In a two-dimensional directed CC network model [9–16], propagation is unidirectional along the horizontal direction and bidirectional along the vertical direction of the two-dimensional network.

To establish this decoupling at $\theta = 0$, we start from

$$\begin{pmatrix} \psi_{1,\uparrow}^{(o)} \\ \psi_{2,\downarrow}^{(o)} \\ \psi_{3,\uparrow}^{(o)} \\ \psi_{4,\downarrow}^{(o)} \end{pmatrix} = S \begin{pmatrix} \psi_{2,\uparrow}^{(i)} \\ \psi_{1,\downarrow}^{(i)} \\ \psi_{4,\uparrow}^{(i)} \\ \psi_{3,\downarrow}^{(i)} \end{pmatrix}, \quad (2.12a)$$

where S takes the limiting form

$$S = e^{+i\phi_0} \begin{pmatrix} r e^{+i\phi_3} \sigma_0 & +t Q \\ -t Q^\dagger & +r e^{-i\phi_3} \sigma_0 \end{pmatrix} \quad (2.12b)$$

with the 2×2 diagonal block

$$Q = \begin{pmatrix} +e^{+i\phi_1} & 0 \\ 0 & -e^{-i\phi_1} \end{pmatrix}. \quad (2.12c)$$

It is then advantageous for our purpose to do a unitary transformation that renders explicit the reducibility of the scattering matrix (2.12) in the spin degrees

of freedom

$$\begin{pmatrix} \psi_{1,\uparrow}^{(o)} \\ \psi_{3,\uparrow}^{(o)} \\ \psi_{2,\downarrow}^{(o)} \\ \psi_{4,\downarrow}^{(o)} \end{pmatrix} = \tilde{S} \begin{pmatrix} \psi_{2,\uparrow}^{(i)} \\ \psi_{4,\uparrow}^{(i)} \\ \psi_{1,\downarrow}^{(i)} \\ \psi_{3,\downarrow}^{(i)} \end{pmatrix}, \quad (2.13a)$$

where \tilde{S} takes the limiting form

$$\tilde{S} = e^{+i\phi_0} \begin{pmatrix} \tilde{Q}(t, \phi_1, \phi_3) & 0 \\ 0 & \tilde{Q}^T(t, \phi_1, \phi_3) \end{pmatrix} \quad (2.13b)$$

with the 2×2 block

$$\tilde{Q}(t, \phi_1, \phi_3) = \begin{pmatrix} +r e^{+i\phi_3} & +t e^{+i\phi_1} \\ -t e^{-i\phi_1} & +r e^{-i\phi_3} \end{pmatrix}. \quad (2.13c)$$

The upper-left and lower-right 2×2 blocks $e^{+i\phi_0} \tilde{Q}(t, \phi_1, \phi_3)$ and $e^{+i\phi_0} \tilde{Q}^T(t, \phi_1, \phi_3)$, respectively, are related by time reversal. Each block defines the elementary scattering matrix of the two-dimensional directed CC network model [10]. It is shown in Ref. [10] (see also Refs. [9,11–16]) that the localization properties of the two-dimensional directed CC network model are the following. Transport is highly anisotropic, for it is perfect along one direction and critical along the orthogonal direction of the two-dimensional network [50]. The fixed point (2.11) is thus the *spin-chiral metallic fixed point*.

3. Limit $r^2 = 0$ without dimerization

We set

$$\delta^2 = r^2 = 0. \quad (2.14)$$

When $r^2 = 0$, the elementary scattering matrix from Eq. (2.3) becomes

$$\begin{pmatrix} \psi_{1,\uparrow}^{(o)} \\ \psi_{2,\downarrow}^{(o)} \\ \psi_{3,\uparrow}^{(o)} \\ \psi_{4,\downarrow}^{(o)} \end{pmatrix} = S \begin{pmatrix} \psi_{2,\uparrow}^{(i)} \\ \psi_{1,\downarrow}^{(i)} \\ \psi_{4,\uparrow}^{(i)} \\ \psi_{3,\downarrow}^{(i)} \end{pmatrix}, \quad (2.15a)$$

where S takes the limiting form

$$S = e^{+i\phi_0} \begin{pmatrix} 0 & +Q(\theta, \phi_1, \phi_2) \\ -Q^\dagger(\theta, \phi_1, \phi_2) & 0 \end{pmatrix} \quad (2.15b)$$

with the 2×2 block

$$Q(\theta, \phi_1, \phi_2) = \begin{pmatrix} +e^{+i\phi_1} \cos \theta & +e^{+i\phi_2} \sin \theta \\ +e^{-i\phi_2} \sin \theta & -e^{-i\phi_1} \cos \theta \end{pmatrix}. \quad (2.15c)$$

We do the unitary transformation

$$\begin{pmatrix} \psi_{1,\uparrow}^{(o)} \\ \psi_{2,\downarrow}^{(o)} \\ \psi_{3,\uparrow}^{(o)} \\ \psi_{4,\downarrow}^{(o)} \end{pmatrix} = \tilde{S} \begin{pmatrix} \psi_{3,\downarrow}^{(i)} \\ \psi_{4,\uparrow}^{(i)} \\ \psi_{1,\downarrow}^{(i)} \\ \psi_{2,\uparrow}^{(i)} \end{pmatrix}, \quad (2.16a)$$

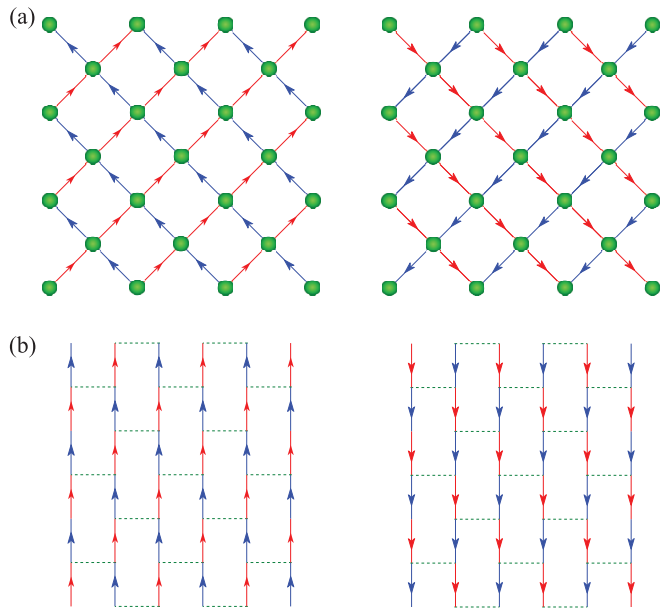


FIG. 10. (Color online) When $\delta^2 = r^2 = 0$, the two-dimensional spin-directed \mathbb{Z}_2 network model from Fig. 6 decouples into two directed CC models that are related by time reversal. Panels (a) and (b) are drawn using the vertex and the brick-wall representations, respectively.

where \tilde{S} takes the limiting form

$$\tilde{S} = e^{+i\phi_0} \begin{pmatrix} \tilde{Q}(\cos \theta, \phi_1, \phi_2) & 0 \\ 0 & \tilde{Q}^T(\cos \theta, \phi_1, \phi_2 + \pi) \end{pmatrix} \quad (2.16b)$$

with the 2×2 block

$$\tilde{Q}(\cos \theta, \phi_1, \phi_2) = \begin{pmatrix} +e^{+i\phi_2} \sin \theta & +e^{+i\phi_1} \cos \theta \\ -e^{-i\phi_1} \cos \theta & +e^{-i\phi_2} \sin \theta \end{pmatrix}. \quad (2.16c)$$

The upper-left and lower-right 2×2 blocks $e^{+i\phi_0} \tilde{Q}(\cos \theta, \phi_1, \phi_2)$ and $e^{+i\phi_0} \tilde{Q}^T(\cos \theta, \phi_1, \phi_2 + \pi)$, respectively, are related by time reversal.

The elementary scattering matrix (2.16) is identical to the elementary scattering matrix (2.13) as implied by the identifications

$$\sin \theta \rightarrow r, \quad \cos \theta \rightarrow t, \quad \phi_2 \rightarrow \phi_3. \quad (2.17)$$

Consequently, the two-dimensional directed \mathbb{Z}_2 network model from Fig. 6 decouples into two directed CC network models that are related by time reversal when $\delta^2 = r^2 = 0$. This decoupling is shown in Fig. 10. Transport is highly anisotropic, for it is perfect along one spanning vector and critical along the second spanning vector of the two-dimensional network. The fixed point (2.14) is thus again the *spin-chiral metallic fixed point*. The relationship between the fixed points (2.14) and (2.11) is that the directions for perfect and critical transport have been interchanged.

4. Limit $\theta = \pi/2$ without dimerization

We set

$$\delta^2 = \theta - \frac{\pi}{2} = 0. \quad (2.18)$$

When $\theta = \pi/2$, the elementary scattering matrix from Eq. (2.3) becomes

$$\begin{pmatrix} \psi_{1,\uparrow}^{(o)} \\ \psi_{2,\downarrow}^{(o)} \\ \psi_{3,\uparrow}^{(o)} \\ \psi_{4,\downarrow}^{(o)} \end{pmatrix} = S \begin{pmatrix} \psi_{2,\uparrow}^{(i)} \\ \psi_{1,\downarrow}^{(i)} \\ \psi_{4,\uparrow}^{(i)} \\ \psi_{3,\downarrow}^{(i)} \end{pmatrix}, \quad (2.19a)$$

where S takes the limiting form

$$S = e^{+i\phi_0} \begin{pmatrix} +r e^{+i\phi_3} \sigma_0 & +t Q \\ -t Q^\dagger & +r e^{-i\phi_3} \sigma_0 \end{pmatrix} \quad (2.19b)$$

with the 2×2 block

$$Q = \begin{pmatrix} 0 & e^{+i\phi_2} \\ e^{-i\phi_2} & 0 \end{pmatrix}. \quad (2.19c)$$

We do the unitary transformation

$$\begin{pmatrix} \psi_{1,\uparrow}^{(o)} \\ \psi_{4,\downarrow}^{(o)} \\ \psi_{2,\downarrow}^{(o)} \\ \psi_{3,\uparrow}^{(o)} \end{pmatrix} = \tilde{S} \begin{pmatrix} \psi_{2,\uparrow}^{(i)} \\ \psi_{3,\downarrow}^{(i)} \\ \psi_{1,\downarrow}^{(i)} \\ \psi_{4,\uparrow}^{(i)} \end{pmatrix}, \quad (2.20a)$$

where \tilde{S} takes the limiting form

$$\tilde{S} = e^{+i\phi_0} \begin{pmatrix} \tilde{Q}(t, \phi_2, \phi_3) & 0 \\ 0 & \tilde{Q}^T(t, \phi_2 + \pi, \phi_3) \end{pmatrix} \quad (2.20b)$$

with

$$\tilde{Q}(t, \phi_2, \phi_3) = \begin{pmatrix} +r e^{+i\phi_3} & +t e^{+i\phi_2} \\ -t e^{-i\phi_2} & +r e^{-i\phi_3} \end{pmatrix}. \quad (2.20c)$$

The upper-left and lower-right 2×2 blocks $e^{+i\phi_0} \tilde{Q}(t, \phi_2, \phi_3)$ and $e^{+i\phi_0} \tilde{Q}^T(t, \phi_2 + \pi, \phi_3)$, respectively, are related by time reversal. Moreover, they are nothing but the elementary scattering matrix for the two-dimensional CC network model that describes the localization properties of the lowest Landau level perturbed by disorder in the integer quantum Hall effect (IQHE). Consequently, the two-dimensional spin-directed \mathbb{Z}_2 network model from Fig. 6 decouples into two CC network models that are related by time reversal when $\delta^2 = \theta - \pi/2 = 0$. This decoupling is shown in Fig. 11.

Chalker and Coddington showed in Ref. [51] that the CC network model is critical if every node of the network is described by the scattering matrix $e^{+i\phi_0} \tilde{Q}(t, \phi_2, \phi_3)$ given in Eq. (2.20c) sharing the same tunneling amplitude t . Hence, the two-dimensional spin-directed \mathbb{Z}_2 network model with $\delta^2 = \theta - \pi/2 = 0$ is always critical. In the special isotropic case when $t^2 = r^2 = \frac{1}{2}$, this critical point is called the *isotropic CC critical point*. In the generic anisotropic case when $t^2 = 1 - r^2 \neq \frac{1}{2}$, this critical point is called the *anisotropic CC critical point*.

5. Phase diagram without dimerization

All four boundaries of parameter space (2.8) shown as the sides of the square in Fig. 12(a) evade localization. Three of these boundaries belong to the unitary class, one

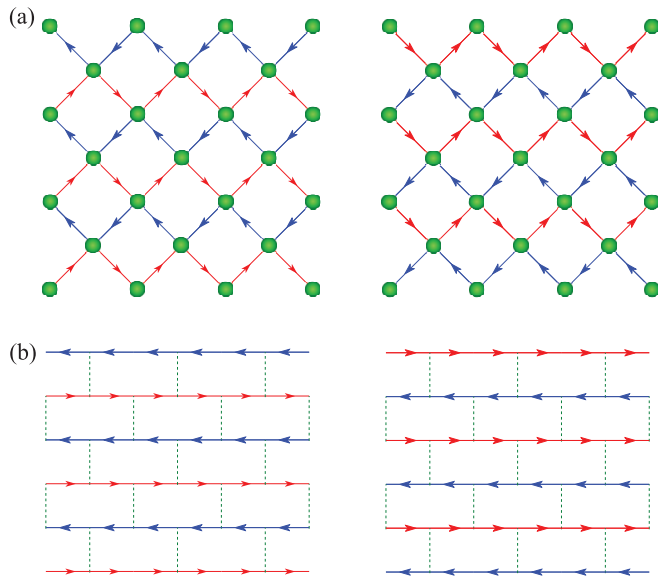


FIG. 11. (Color online) When $\delta^2 = \theta - \pi/2 = 0$, the two-dimensional spin-directed \mathbb{Z}_2 network model from Fig. 6 decouples into two directed CC network models that are related by time reversal. Panels (a) and (b) are drawn using the vertex and the brick-wall representations, respectively. Since all elementary scattering 2×2 blocks in Eq. (2.20) are the same, criticality holds for any $0 \leq t^2 \leq 1$. At the isotropic point $t^2 = r^2 = \frac{1}{2}$, the system exhibits the criticality of the usual isotropic CC model, otherwise, the system exhibits the critical behavior of the anisotropic CC model.

to the symplectic class. Any deviation away from these boundaries puts the two-dimensional spin-directed \mathbb{Z}_2 network model in the two-dimensional symplectic class of Anderson localization. The symplectic class for disordered metals is the most robust to the effects of disorder in that it displays the phenomenon of weak antilocalization for any dimensionality, i.e., the perturbative effect of disorder in the diffusive metallic regime is to enhance the conductivity in the symplectic class [52]. Hence, the most economical conjecture regarding the nature of the interior of parameter space (2.8) with regard to the physics of localization is that it is metallic. This scenario is confirmed by our numerical calculations that we present in Sec. III except for the region where $t^2 \ll 1$. Although the numerical results in this region are inconclusive, we argue in favor of a metallic phase. In fact, the effective Dirac Hamiltonian derived for $t^2 \ll 1$ in Appendix A is nothing but the Hamiltonian studied by Mong *et al.* [36] with additional anisotropy in velocities. Their numerical results imply that this region of question is metallic. We can thus conclude that there is only a metallic phase in the interior of the square in Fig. 12(a).

6. Phase diagram with dimerization

We close Sec. II with the summary of our numerical results, to be described in more detail in Sec. III, in the form of the cuts of the schematic three-dimensional phase diagram displayed in Fig. 12(c).

Any nonvanishing dimerization δ^2 shrinks parameter space (2.8) through the condition

$$\delta^2 \leq t^2 \leq 1 - \delta^2. \quad (2.21)$$

According to Appendix B, the continuum limit of the two-dimensional spin-directed \mathbb{Z}_2 network model in the vicinity of $\theta = 0$ is that of a gapless Hamiltonian for any allowed value of t^2 and δ^2 in the three-dimensional parameter space (2.7). Hence, we anticipate a metallic phase when $\theta = 0$ in the three-dimensional parameter space (2.7). According to Appendix B, the continuum limit of the two-dimensional spin-directed \mathbb{Z}_2 network model in the vicinity of $\theta = \pi/2$ is that of a massive Dirac equation for any allowed value of t^2 and $\delta^2 \neq 0$ in the three-dimensional parameter space (2.7). Hence, we anticipate an insulating phase when $\theta = \pi/2$ and $\delta^2 \neq 0$ in the three-dimensional parameter space (2.7). Incidentally, a numerical study of two-component Dirac fermions with random mass and random potentials from Ref. [53] supports this conclusion.

On the boundary $0 \leq t^2 = \delta^2 \leq \frac{1}{2}$ of the three-dimensional parameter space (2.7), Eq. (2.5) implies that the two values taken by the dimerized hopping are $t_+^2 = 2t^2$ and $t_-^2 = 0$, respectively. Correspondingly (recall Fig. 2), the network model effectively describes the one-dimensional propagation of two Kramers' degenerate pairs of helical edge states on this boundary. Hence, this boundary, if supplemented by the condition $\theta = 0$, is the end line of a critical surface at which a metal-insulator transition takes place in the three-dimensional parameter space (2.7). On the insulating side of this quantum phase transition, dimerization is strong relative to the disorder strength in that the density of states is so low in the presence of disorder that localization rules. On the metallic side of this quantum phase transition, dimerization is weak relative to the disorder strength in that the metallic fixed point in the two-dimensional symplectic symmetry class of Anderson localization is realized.

On the boundary $\frac{1}{2} \leq t^2 = 1 - \delta^2 \leq 1$ of the three-dimensional parameter space (2.7), Eq. (2.5) implies that the two values taken by the dimerized hopping are $t_+^2 = 1$ and $t_-^2 = 2t^2 - 1$, respectively. Correspondingly (recall Fig. 2), the network model effectively describes the one-dimensional propagation of two Kramers' degenerate pairs of helical edge states only at the point $t^2 = \delta^2 = \frac{1}{2}$ on this boundary. Hence, the localization properties of surface states on this boundary can not be deduced by mere inspection. We expect a metal-insulator transition driven by θ , for the surface states are extended on the boundary $\theta = 0$, while they are localized on the boundary $\theta = \pi/2$. Finally, upon increasing δ^2 towards $\frac{1}{2}$, the critical point $\theta_c(\delta^2)$ at which the metal-insulator transition takes place should decrease since transport is effectively one dimensional at $\delta^2 = \frac{1}{2}$. A qualitative numerical study of the localization properties along the boundary $\frac{1}{2} \leq t^2 = 1 - \delta^2 \leq 1$ can be found at the end of Sec. III E.

From these considerations, we conjecture the schematic three-dimensional phase diagram shown in Fig. 12(c). We now present numerical support for the phase diagram 12(c).

III. NUMERICAL DATA FOR AN EVEN NUMBER OF DIMERIZED CHANNELS

A. Transfer matrix

In numerical studies of network models, it is convenient to do a similarity transformation on the space of scattering states. Instead of defining a two-dimensional spin-directed \mathbb{Z}_2

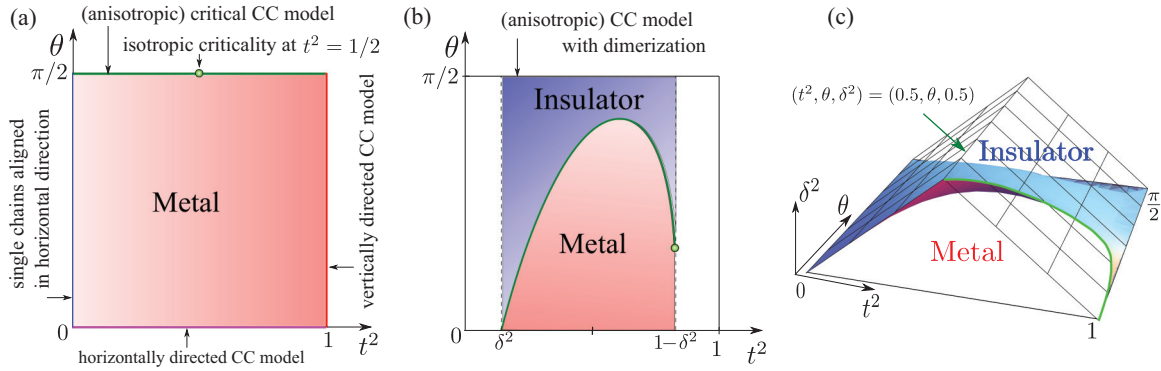


FIG. 12. (Color online) (a) Phase diagram in the two-dimensional parameter space (a square) (2.8) without dimerization of the two-dimensional spin-directed \mathbb{Z}_2 network model. The boundaries of the square correspond to a two-dimensional chiral metal when $\theta = 0$, a two-dimensional chiral metal when $t = 1$, the metal-insulator critical point of the (two-dimensional) CC model when $\theta = \pi/2$, and the quasi-one-dimensional symplectic metallic fixed point when $t^2 = 0$. Numerics of the two-dimensional spin-directed \mathbb{Z}_2 network model are consistent with a metallic phase in the interior of the square except in the region of $t^2 \ll 1$ for which numerics are inconclusive. However, we show in Appendix A that the numerical results from Ref. [36] apply to this region, thereby implying that this region is metallic. (b) Two-dimensional cut of the phase diagram in the three-dimensional parameter space (2.7) with *fixed and nonvanishing* dimerization of the two-dimensional spin-directed \mathbb{Z}_2 network model. The green dot is on the boundary $\frac{1}{2} \leq t^2 = 1 - \delta^2 \leq 1$ of the three-dimensional parameter space (2.7). The presence of the dimerization improves the quality of the numerics. Dimerization reduces the area of the metallic phase. The divergences of the localization length at the metal-insulator transitions are consistent with a metal-insulator critical point belonging to the two-dimensional symplectic class of Anderson localization. (c) Qualitative phase diagram in the three-dimensional parameter space (2.7) with *fixed and nonvanishing* dimerization. The phase boundary represented by the green curve is on the boundary $\frac{1}{2} \leq t^2 = 1 - \delta^2 \leq 1$ of the three-dimensional parameter space (2.7). The phase diagram that includes the effect of the sign of the dimerization in Eq. (2.7) can be represented by gluing along the negative δ^2 axis the mirror image about the plane $\delta^2 = 0$ of the phase diagram for positive δ^2 . This delivers two insulating phases separated by a metallic phase.

network model by a unitary scattering matrix that maps $2M$ incoming plane waves into $2M$ outgoing plane waves, we can do a similarity transformation on the scattering states under which a unitary scattering matrix turns into a pseudounitary transfer matrix. The transfer matrix maps the plane waves at the bottom of the brick wall to the plane waves at the

top of the brick wall if the boundary conditions are those of Fig. 13(a). If the boundary conditions are those of Fig. 13(b), the transfer matrix maps the plane waves at the left of the brick wall to the plane waves at the right of the brick wall. In the former case, the elementary transfer matrix is defined by

$$\begin{pmatrix} \psi_{2,\uparrow}^{(i)} \\ \psi_{1,\downarrow}^{(i)} \\ \psi_{1,\uparrow}^{(o)} \\ \psi_{2,\downarrow}^{(o)} \end{pmatrix} = \mathcal{M}_\perp \begin{pmatrix} \psi_{4,\uparrow}^{(i)} \\ \psi_{3,\downarrow}^{(i)} \\ \psi_{3,\uparrow}^{(o)} \\ \psi_{4,\downarrow}^{(o)} \end{pmatrix}, \quad \mathcal{M}_\perp := \begin{pmatrix} +\frac{r}{t} e^{-i\phi_3} Q & -\frac{1}{t} e^{-i\phi_0} Q \\ +\frac{1}{t} e^{+i\phi_0} Q & -\frac{r}{t} e^{+i\phi_3} Q \end{pmatrix}. \quad (3.1)$$

In the latter case, the elementary transfer matrix is defined by

$$\begin{pmatrix} \psi_{1,\uparrow}^{(o)} \\ \psi_{3,\uparrow}^{(o)} \\ \psi_{1,\downarrow}^{(i)} \\ \psi_{3,\downarrow}^{(i)} \end{pmatrix} = \mathcal{M}_\parallel \begin{pmatrix} \psi_{2,\uparrow}^{(i)} \\ \psi_{4,\uparrow}^{(i)} \\ \psi_{2,\downarrow}^{(o)} \\ \psi_{4,\downarrow}^{(o)} \end{pmatrix}, \quad (3.2a)$$

where

$$\mathcal{M}_\parallel := \frac{1}{r^2 + t^2 \cos^2 \theta} \begin{pmatrix} r e^{+i(\phi_0 + \phi_3)} & t e^{+i(\phi_0 + \phi_1)} \cos \theta & -t^2 e^{+i(\phi_1 + \phi_2)} \sin \theta \cos \theta & r t e^{+i(\phi_2 + \phi_3)} \sin \theta \\ -t e^{+i(\phi_0 - \phi_1)} \cos \theta & r e^{+i(\phi_0 - \phi_3)} & -r t e^{+i(\phi_2 - \phi_3)} \sin \theta & -t^2 e^{-i(\phi_1 - \phi_2)} \sin \theta \cos \theta \\ t^2 e^{-i(\phi_1 + \phi_2)} \sin \theta \cos \theta & -r t e^{-i(\phi_2 + \phi_3)} \sin \theta & r e^{-i(\phi_0 + \phi_3)} & t e^{-i(\phi_0 + \phi_1)} \cos \theta \\ r t e^{-i(\phi_2 - \phi_3)} \sin \theta & t^2 e^{+i(\phi_1 - \phi_2)} \sin \theta \cos \theta & -t e^{-i(\phi_0 - \phi_1)} \cos \theta & r e^{-i(\phi_0 - \phi_3)} \end{pmatrix}. \quad (3.2b)$$

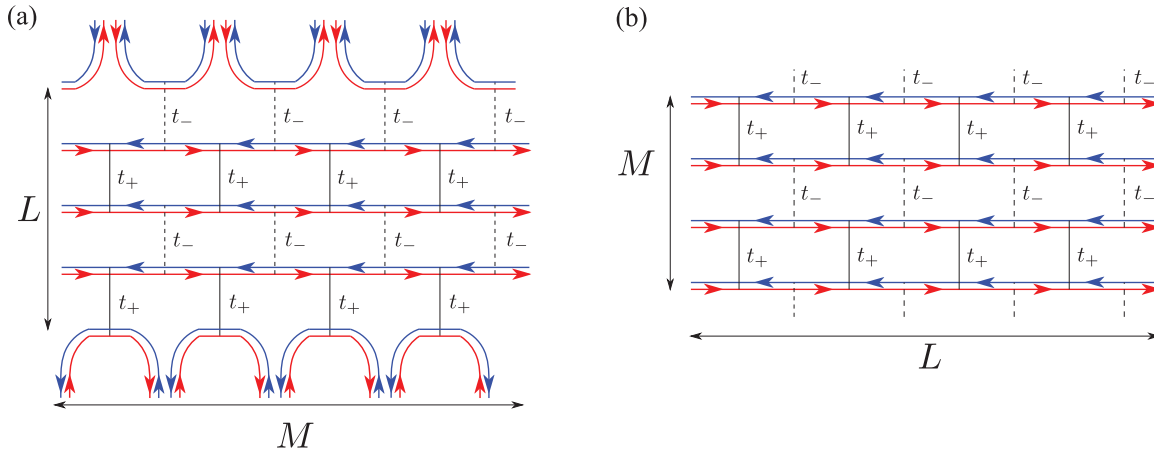


FIG. 13. (Color online) Two examples in the brick-wall representation of two-dimensional spin-directed \mathbb{Z}_2 network models built out of the elementary scattering processes shown in Fig. 5. The periodic choice of the transmission amplitudes t_+ and t_- implements a dimerization pattern. The red and blue lines represent the flow of electron with up and down spins, respectively. The continuous (dotted) black line represents the scattering with transmission amplitude t_+ (t_-) between them. Periodic boundary conditions are imposed along the horizontal and vertical directions in panels (a) and (b), respectively. The dimensions of these two-dimensional spin-directed \mathbb{Z}_2 network models are $M \times L = 8 \times 4$ and $L \times M = 8 \times 4$ for examples (a) and (b), respectively.

We refer the reader to Ref. [42] for the detailed construction of the total transfer matrix \mathcal{M}_{tot} corresponding to Fig. 13 from the elementary 4×4 transfer matrix of Eq. (3.2).

B. Definition of the normalized localization length

As explained in Ref. [42], the transfer matrix \mathcal{M}_{tot} is pseudounitary and belongs to the group $\text{SO}^*(2M)$ given the definition of M in Fig. 13 (M is even). The matrix $\mathcal{M}_{\text{tot}}^\dagger \mathcal{M}_{\text{tot}}$ built up from \mathcal{M}_x with $x = \perp$ or \parallel is positive definite and has the doubly degenerate eigenvalues of the form $\exp(\pm 2X_{x,j})$ with $j = 1, \dots, M/2$, which can be ordered according to the convention

$$0 < X_{x,1} < \dots < X_{x,M/2}. \quad (3.3)$$

The ordered numbers $X_{x,j}$ with $j = 1, \dots, M/2$ are called Lyapunov exponents. They become self-averaging random variables as the quasi-one-dimensional limit $L \rightarrow \infty$ for fixed M is taken in Fig. 13 [54]. The quasi-one-dimensional localization length is defined by

$$\xi_{x,M} := \lim_{L \rightarrow \infty} \frac{L}{X_{x,1}}. \quad (3.4)$$

As shown by MacKinnon and Kramer [55], criticality in two dimensions can be probed through the dependence of the normalized localization length

$$\Lambda_x := \frac{\xi_{x,M}}{M} \quad (3.5)$$

on the width M of the quasi-one-dimensional spin-directed network model in Fig. 13. We are going to study numerically the dependence on M of the normalized localization lengths Λ_\perp and Λ_\parallel defined by the geometries of Figs. 13(a) and 13(b), respectively. To this end, we shall use the transfer matrix method from Ref. [55] in a quasi-one-dimensional geometry with the aspect ratio $L/M = 5 \times 10^5$. We work in the parameter space (2.7).

C. Finite-size scaling analysis

We apply a finite-size scaling analysis to the normalized localization lengths Λ_\perp and Λ_\parallel with the goal of studying the critical properties at the metal-insulator transition of the two-dimensional spin-directed \mathbb{Z}_2 network model, if any. To this end, the normalized localization lengths along the vertical Λ_\perp and horizontal Λ_\parallel directions of the two-dimensional network are calculated numerically by the transfer matrix method [55] as a function of δ^2 with fixed values of the intrinsic parameters t^2 and θ and the geometric parameter M , whereby the width M ranges from a minimal value M_{min} to a maximal value M_{max} .

We extract the critical exponent ν for the power-law divergence of the localization length defined by

$$\xi \propto |z - z_c|^{-\nu}, \quad (3.6)$$

where z and z_c denote any relevant parameter driving to the metal-insulator transition and its critical point, respectively. In this work, we choose the parameter z that controls the distance to the critical point z_c out of δ^2 , θ , $\delta\phi$, and t^2 defined in Eq. (2.6). It is well known that the normalized localization length near the Anderson transition obeys a scaling law (not necessarily a power law, though) [55].

We treat the scaling behavior of the inverse

$$\Gamma_x := \Lambda_x^{-1}, \quad x \equiv \perp, \parallel \quad (3.7)$$

of the normalized localization length Λ_x , which is proportional to the Lyapunov exponent $X_{x,1}$, a random variable that is self-averaging in the thermodynamic limit [54]. The error bars on Γ_x are easier to obtain than the error bars on Λ_x .

We assume that Γ_x is a scaling function [56]

$$\Gamma_x = F_x(\eta M^{1/\nu}, \zeta M^y), \quad (3.8)$$

where η and ζ are the relevant and first leading irrelevant scaling variables, respectively. The irrelevant exponent y satisfies $y < 0$. In the limit $M \rightarrow \infty$, we furthermore assume that the scaling law (3.8) obeys a Taylor expansion in powers

of the scaling fields η and ζ about $\eta M^{1/\nu} = \zeta M^y = 0$ that we truncate to the order N_{rel} and $N_{\text{irr}}(p)$, respectively,

$$\Gamma_x \approx \sum_{p=0}^{N_{\text{rel}}} \sum_{q=0}^{N_{\text{irr}}(p)} F_x^{p,q} \eta^p \zeta^q M^{p/\nu+qy}, \quad (3.9)$$

where $F_x^{p,q}$ is the expansion coefficient at the p th and q th order of $\eta M^{1/\nu}$ and ζM^y , respectively. Here, we have allowed for the possibility that $N_{\text{irr}}(p)$ depends on p . If we assume that the expansion coefficients $F_x^{p,0}$ are all nonvanishing, we may then do the factorization

$$\Gamma_x \approx \sum_{p=0}^{N_{\text{rel}}} F_x^{p,0} (\eta M^{1/\nu})^p \left[1 + \sum_{q=1}^{N_{\text{irr}}(p)} f_x^{p,q} (\zeta M^y)^q \right],$$

$$f_x^{p,q} := \frac{F_x^{p,q}}{F_x^{p,0}}. \quad (3.10)$$

It is an empirical fact that the fitting procedure (3.10) is more stable than the fitting procedure (3.9). Finally, we assume that

$$\eta := z - z_c, \quad (3.11)$$

where z and z_c were introduced in Eq. (3.6) and

$$\zeta = 1. \quad (3.12)$$

In other words, we choose as the fitting parameters (1) the scaling exponents ν and y , (2) the location of the critical point z_c , (3) the $(N_{\text{rel}} + 1)$ expansion coefficients for the relevant perturbation $F_x^{p,0}$ for $p = 0, \dots, N_{\text{rel}}$, and (4) the $\sum_{p=0}^{N_{\text{rel}}} N_{\text{irr}}(p)$ expansion coefficients for the leading irrelevant perturbation $f_x^{p,q}$ for $q = 1, \dots, N_{\text{irr}}(p)$ and $p = 0, \dots, N_{\text{rel}}$. We call

$$\Lambda_x^c := \frac{1}{F_x^{0,0}} \quad (3.13)$$

the universal scaling amplitude of the normalized localization lengths with $x = \perp, \parallel$, respectively. In order to demonstrate a single-parameter scaling law, we introduce

$$\Lambda_x' := (\Gamma_x')^{-1}, \quad x = \perp, \parallel \quad (3.14a)$$

where Γ_x' is defined by subtracting from Γ_x its finite-size correction from the leading irrelevant exponent y , i.e.,

$$\Gamma_x' := \Gamma_x - \sum_{p=0}^{N_{\text{rel}}} \sum_{q=1}^{N_{\text{irr}}(p)} F_x^{p,0} f_x^{p,q} (\eta M^{1/\nu})^p M^{qy}. \quad (3.14b)$$

The quality of the fit of the data set to the scaling function is tested as follows. The simplest test for fitting numerical data is given by

$$\frac{\chi^2}{N} := \frac{1}{N} \sum_{j=1}^N \frac{(O_j - E_j)^2}{\sigma^2}, \quad (3.15)$$

where $O_j (= \Gamma_x)$ runs over the N data, σ^2 is the variance of the data, and E_j is the value of the fitting function computed from Eq. (3.10) corresponding to data O . The values of χ^2/N are distributed in the range $[0, \infty[$, and a perfect fit gives $\chi^2/N = 0$. In practice, a fit is acceptable if χ^2/N is smaller than 1.

Another measure for the quality of the fitting procedure is the goodness of fit \mathcal{G} defined by

$$\mathcal{G} := \Gamma_{\text{ni}}((N-p)/2, \chi^2/2), \quad (3.16a)$$

where

$$\Gamma_{\text{ni}}(a, x) := \frac{1}{\Gamma(a)} \int_x^\infty dy y^{a-1} e^{-y} \quad (3.16b)$$

denotes the normalized incomplete gamma function. The values of \mathcal{G} are distributed in the range $[0, 1]$. A perfect fit gives $\mathcal{G} = 1$.

A consistency check on the fitting procedure is obtained by verifying that the statistical error bar (one sigma) on a fitting parameter does not exceed the value of the fitting parameter by an order of magnitude. Error bars of fitting parameters are themselves estimated from error-propagation theory given the error bars of Λ_x .

The fitting with the nonlinear function (3.10) strongly depends on the initial values of the fitting parameters. For this reason, we perform iteratively the fitting for the data set with different initial values of the fitting parameters. We then select the best fitting parameters as the ones with the smallest value of χ^2/N , that we denote χ_{min}^2/N . The best fitting parameters and their χ_{min}^2/N define the most reliable fit for a given data set. The typical number of iterations done for a given data set is about 1000.

The best fitting parameters should not strongly depend on the given data set. For this reason, we repeat our scaling analysis for data sets differing through the choice of their minimum and maximum values M_{min} and M_{max} for the width of the quasi-one-dimensional spin-directed \mathbb{Z}_2 network model. As we demonstrate later, the fitting parameters obtained from data sets with different minimum M_{min} and maximum M_{max} widths are not always consistent with each other. To overcome this difficulty, we estimate the error bars on the fitting parameters by making use of the practical-error-bar procedure from Ref. [57].

D. Dependence of the normalized localization length on δ^2

To begin with, we choose the one-dimensional cut

$$A: (0.5, \pi/4, \delta^2), \quad \delta^2 \in [0, 0.5] \quad (3.17)$$

of three-dimensional parameter space (2.7). Cut A is shown in Fig. 14 with the label ‘‘A.’’ This cut is far from the isotropic CC critical point

$$(0.5, \pi/2, 0). \quad (3.18)$$

Figures 15(a-1) and 15(b-1) show the δ^2 dependence of the normalized localization lengths Λ_\perp and Λ_\parallel defined by the geometries of Figs. 13(a) and 13(b), respectively, along the cut (3.17) as the width M is increased from $M = 16$ to 320. According to Fig. 15(a-1), Λ_\perp and Λ_\parallel increase (decrease) with increasing M for small (large) values of δ^2 . The dependence on M of either Λ_\perp or Λ_\parallel appears to vanish at a value of δ^2 approximately given by 0.23. This suggests that the point

$$(t_c^2, \theta_c, \delta_c^2) := (0.5, \pi/4, 0.23) \quad (3.19)$$

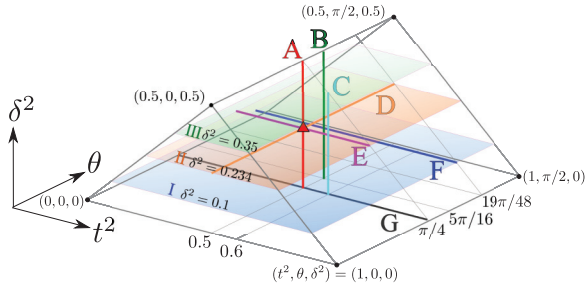


FIG. 14. (Color online) One and two-dimensional cuts in the parameter space (2.7) studied in this paper. The one-dimensional cuts, A defined in Eq. (3.17), B in (3.20), C in (3.21), D in (3.23), E in (3.26), F in (3.27), and G in (3.28), as well as the two-dimensional cuts, I–III, defined in Eq. (3.25) are shown. The red triangle where the three one-dimensional cuts A, D, and E cross represents the critical point (3.19).

in the three-dimensional parameter space (2.7) is a critical point at which a metal-insulator transition takes place.

1. Finite-size scaling for the normalized localization length with dimerization

To confirm this interpretation of the point (3.19) in the three-dimensional parameter space (2.7), we have done a finite-size scaling analysis of the data presented in Figs. 15(a-1) and 15(b-1) by regarding δ^2 as the driving parameter z in Eq. (3.6), the details of which are to be found in Tables I–III (from Appendix C for Tables II and III).

Figures 15(a-2) and 15(b-2) support the one-parameter scaling obeyed by Λ'_\perp and Λ'_\parallel in Eqs. (3.14a) and (3.14b) close to the critical point (3.19) in the three-dimensional parameter space (2.7). We use values of the irrelevant exponent y and the expansion coefficient $f_x^{p,q}$ given in Tables II and III to calculate Λ'_\perp and Λ'_\parallel through Eqs. (3.14a) and (3.14b).

As is reported in Tables II and III, the fitting parameters obtained by varying the minimum and maximum widths M_{\min} and M_{\max} , respectively, are not always consistent with the statistical error bars, even though χ^2_{\min}/N and \mathcal{G} are acceptable. On the one hand, Table II gives values of ν from all data sets that vary within the statistical error bars. On the other hand, Table III gives values of ν extracted from the data set

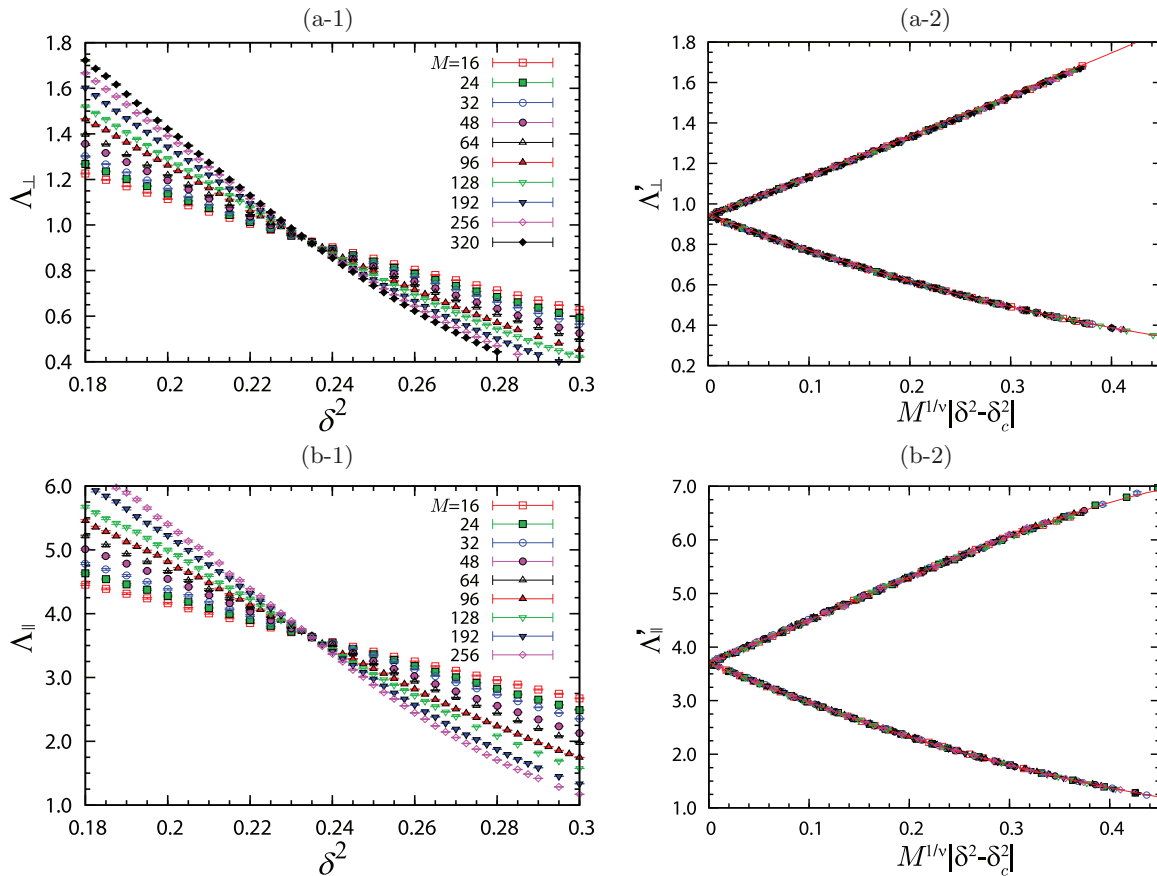


FIG. 15. (Color online) The two-dimensional spin-directed \mathbb{Z}_2 network model is solved numerically along the one-dimensional cut (3.17) in the three-dimensional parameter space (2.7). Panel (a-1) shows the δ^2 dependence of the normalized localization length Λ_\perp corresponding to the geometry of Fig. 13(a) for several values of M . Panel (b-1) shows the δ^2 dependence of the normalized localization lengths Λ_\parallel corresponding to the geometry of Fig. 13(b) for several values of M . A finite-size scaling analysis of panels (a-1) and (b-1) is performed in panels (a-2) and (b-2), respectively. The horizontal axis is $M^{1/\nu}|\delta^2 - \delta_c^2|$ with ν and δ_c^2 given in Tables II and III in Appendix C. The vertical axis Λ'_x with $x = \perp, \parallel$ is defined by subtracting from the normalized localization length Λ_x its finite-size correction from the leading irrelevant exponent y given in Tables S-I and S-II from Ref. [45]. The red solid curve demonstrates the quality of the data collapse onto a one-parameter scaling function.

TABLE I. Summary of the finite-size scaling analysis for $\Gamma_x (=1/\Lambda_x)$ with $x = \perp, \parallel$ for the three cuts (3.17), (3.20), and (3.21) from the three-dimensional parameter space (2.7). Only the most important fitting parameters, namely, ν , y , δ_c^2 , Λ_x^c , and $\sqrt{\Lambda_\perp^c \Lambda_\parallel^c}$, are shown. More details on this finite-size scaling analysis can be found in Tables II–VII in Appendix C. The expected value and its error bar are estimated by employing the practical error-bar procedure [57].

x	θ	t^2	ν	$ y $	δ_c^2	Λ_x^c	$\sqrt{\Lambda_\perp^c \Lambda_\parallel^c}$
\perp	$\pi/4$	0.5	2.89 [2.75 : 2.98]	0.72 [0.59 : 0.90]	0.2340 [0.2334 : 0.2349]	0.935 [0.919 : 0.944]	1.849
\parallel	$\pi/4$	0.5	2.71 [2.53 : 2.85]	0.47 [0.30 : 0.81]	0.2343 [0.2332 : 0.2355]	3.657 [3.557 : 3.734]	
\perp	$5\pi/16$	0.5	2.80 [2.64 : 2.91]	0.91 [0.55 : 1.49]	0.1591 [0.1579 : 0.1616]	1.290 [1.234 : 1.310]	1.850
\parallel	$5\pi/16$	0.5	2.63 [2.55 : 2.79]	1.14 [0.55 : 1.54]	0.1590 [0.1575 : 0.1598]	2.652 [2.622 : 2.716]	
\perp	$\pi/4$	0.6	2.84 [2.70 : 2.92]	0.81 [0.51 : 1.21]	0.2765 [0.2752 : 0.2784]	1.225 [1.193 : 1.249]	1.834
\parallel	$\pi/4$	0.6	2.57 [2.42 : 2.74]	0.85 [0.26 : 1.72]	0.2764 [0.2754 : 0.2772]	2.746 [2.710 : 2.783]	

with $M_{\min} = 16$ and $M_{\max} = 256$ that are not within the error bars from the values of ν extracted from the data set with $M_{\min} = 32$ and $M_{\max} = 256$, while both sets of values are statistically reliable as measured by χ_{\min}^2/N . We believe that the reason for this inconsistency originates from the orders of truncations N_{rel} and $N_{\text{irr}}(p)$ in Eq. (3.10), constrained as they are by the accuracy of our data, being too small. To overcome this difficulty, we estimate the error bars on the fitting parameters shown in Table I by making use of the practical-error-bar procedure from Ref. [57]. The first two lines of Table I give, at the critical point (3.19) along the cut (3.17), the value of the critical exponent ν that controls the power-law divergence of the localization length, the value $|y|$ for the leading irrelevant scaling exponent y , the strength of δ_c^2 , the values of the normalized localization length Λ_\perp^c and Λ_\parallel^c , and their geometrical mean $\sqrt{\Lambda_\perp^c \Lambda_\parallel^c}$.

The subsequent two pairs of lines from Table I summarize the results of the same analysis performed along the one-dimensional cuts

$$\text{B : } (0.5, 5\pi/16, \delta^2), \quad \delta^2 \in [0, 0.5] \quad (3.20)$$

and

$$\text{C : } (0.6, \pi/4, \delta^2), \quad \delta^2 \in [0, 0.4] \quad (3.21)$$

in the three-dimensional parameter space (2.7). Cuts B and C are shown in Fig. 14 with the labels ‘‘B’’ and ‘‘C.’’ The details of the finite-size scaling analysis along the cuts ‘‘B’’ and ‘‘C’’ are presented in Tables IV–VII from Appendix C, respectively. The δ^2 dependence of the normalized localization lengths Λ_\perp and Λ_\parallel for the cuts ‘‘B’’ and ‘‘C’’ are shown in Figs. 26 and 27 from Appendix C, respectively.

The value for the critical point δ_c along a one-dimensional cut with t^2 and θ fixed in the three-dimensional parameter space (2.7) obtained from Λ_\perp agrees within error bars with that obtained from Λ_\parallel . This agreement is required if $(t^2, \theta, \delta_c^2)$ is to be interpreted as a quantum critical point in Anderson localization.

We find the values of the scaling exponent ν to be distributed around 2.7 ± 0.2 in Table I. For comparison, the scaling exponent ν for the ordinary two-dimensional symplectic class is $\nu \approx 2.7$ [58].

In contrast, we observe that the normalized localization lengths at the critical points Λ_\perp^c and Λ_\parallel^c along a given one-dimensional cut in the three-dimensional parameter space (2.7) from Table I differ. These values also differ along

different cuts in the three-dimensional parameter space (2.7) as well as from the value $\Lambda^c \approx 1.84$ obtained for the ordinary two-dimensional symplectic class in Ref. [58]. However, if we take the geometric average of Λ_\perp^c and Λ_\parallel^c , we find that the value

$$\sqrt{\Lambda_\perp^c \Lambda_\parallel^c} \approx 1.84 \quad (3.22)$$

agrees with Λ^c . The result that the geometric average of Λ_\perp^c and Λ_\parallel^c for the two-dimensional spin-directed \mathbb{Z}_2 network model agrees with the value Λ^c for the two-dimensional \mathbb{Z}_2 network model from Ref. [42] has a counterpart for the CC network model. In the anisotropic CC network model defined by the condition $0 \leq t^2 \neq \frac{1}{2} \leq 1$, there are two normalized localization lengths Λ_\perp^c and Λ_\parallel^c whose geometric average equals the normalized localization length of the isotropic CC network model defined by the condition $t^2 = \frac{1}{2}$ [51]. In either case, this relation is a manifestation of two-dimensional conformal invariance at a critical point [59].

The difference between Λ_\perp^c and Λ_\parallel^c along the cut (3.20) is smaller than that along the cut (3.17). This observation is consistent with the fact that the former cut is closer than the latter cut to the isotropic CC critical point (3.18).

The difference between Λ_\perp^c and Λ_\parallel^c along the cut (3.21) is smaller than that along the cut (3.17). We attribute this fact to the property that increasing small t increases Λ_\perp , while it decreases Λ_\parallel .

From these observations, we conjecture that the surface states of weak three-dimensional \mathbb{Z}_2 topological insulators undergo a metal-insulator transition as a result of the competition between disorder and dimerization that belongs to the ordinarily two-dimensional symplectic universality class.

E. Dependence of the normalized localization length on θ

We are going to study the dependence on θ of the normalized localization lengths Λ_\perp and Λ_\parallel , whereby we recall that θ encodes the strength of the spin-orbit couplings.

We first choose the one-dimensional cut

$$\text{D : } (0.5, \theta, 0.234), \quad \theta \in [0, \pi/2] \quad (3.23)$$

of the three-dimensional parameter space (2.7). Cut D is shown in Fig. 14 with the label ‘‘D.’’ Figures 16(a) and 16(b) show the normalized localization lengths Λ_\perp and Λ_\parallel , respectively, as a function of θ along the cut (3.23). We note that, along the cut (3.23), there is the critical point

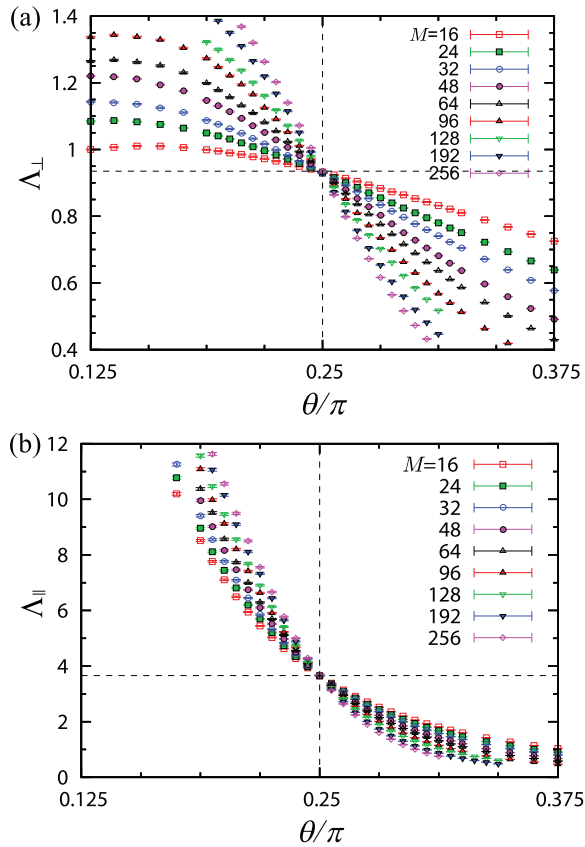


FIG. 16. (Color online) The θ dependence of the normalized localization lengths Λ_{\perp} in panel (a) and Λ_{\parallel} in panel (b) of the two-dimensional spin-directed \mathbb{Z}_2 network model with dimerization along the one-dimensional cut (3.23). The strength of the spin-orbit coupling θ is varied given the values $t^2 = 0.5$ and $\delta^2 = 0.234$ for fixed M ranging from 16 to 256. The vertical and horizontal dashed lines represent θ_c and $\Lambda_{x,c}$, respectively, as deduced from the finite-size scaling analysis summarized in Table I.

$(0.5, \pi/4, 0.234)$ of Eq. (3.19) identified in Sec. III D. The dependence of the normalized localization lengths Λ_{\perp} and Λ_{\parallel} on the width M depicted in Fig. 16 shows the expected metallic behavior for $\theta < \pi/4$ and the expected insulating behavior for $\theta > \pi/4$ from the phase diagram 12(c). We

apply the finite-size scaling analysis by using the data points presented in Fig. 16(b) by choosing θ as the driving parameter z in Eq. (3.6). To improve the stability of the finite-size scaling analysis with the number of data points at our disposal, we have used $\theta_c = \pi/4$ and $\Lambda_c = 3.657$ as given in the scaling function (3.10). The parameter sets used in the finite-size scaling analysis is shown in Table VIII from Appendix C. Applying the practical error-bar procedure [57], we obtain

$$\nu = 2.88 \quad [2.81 : 2.98]. \quad (3.24)$$

This result suggests that the strength of the spin-orbit couplings is also a control parameter that drives the surface states of weak three-dimensional \mathbb{Z}_2 topological insulators through the metal-insulator transition belonging to the ordinary two-dimensional symplectic universality class among the Anderson transitions.

We proceed with the numerical exploration of the three-dimensional parameter space (2.7) depicted in Fig. 12(c) with the three two-dimensional cuts

$$\text{I : } (t^2, \theta, 0.1), \quad t^2 \in [0.1, 0.9], \quad \theta \in [0, \pi/2], \quad (3.25a)$$

$$\text{II : } (t^2, \theta, 0.234), \quad t^2 \in [0.234, 0.766], \quad \theta \in [0, \pi/2], \quad (3.25b)$$

$$\text{III : } (t^2, \theta, 0.35), \quad t^2 \in [0.35, 0.65], \quad \theta \in [0, \pi/2], \quad (3.25c)$$

which are shown in Fig. 14 with the labels ‘‘I,’’ ‘‘II,’’ and ‘‘III,’’ respectively.

We have calculated the normalized localization length Λ_{\parallel} on any one of the two-dimensional cuts I, II, and III. We have estimated the positions (t_c^2, θ_c) of the critical points from the θ dependence of the normalized localization length Λ_{\parallel} at fixed t^2 by using the scaling function (3.10), but neglecting corrections involving the irrelevant exponent y . Because of this simplification, the goodness of fit \mathcal{G} defined in Eq. (3.16) is almost zero so that the obtained values of ν are not reliable. Nevertheless, we believe that the accuracy of the positions of the critical point (t_c^2, θ_c) is sufficient to confirm the phase diagram 12(c). Figures 17(a)–17(c) show the phase diagrams on the two-dimensional cuts I, II, and III, respectively. We find that the metallic phase survives along the boundary

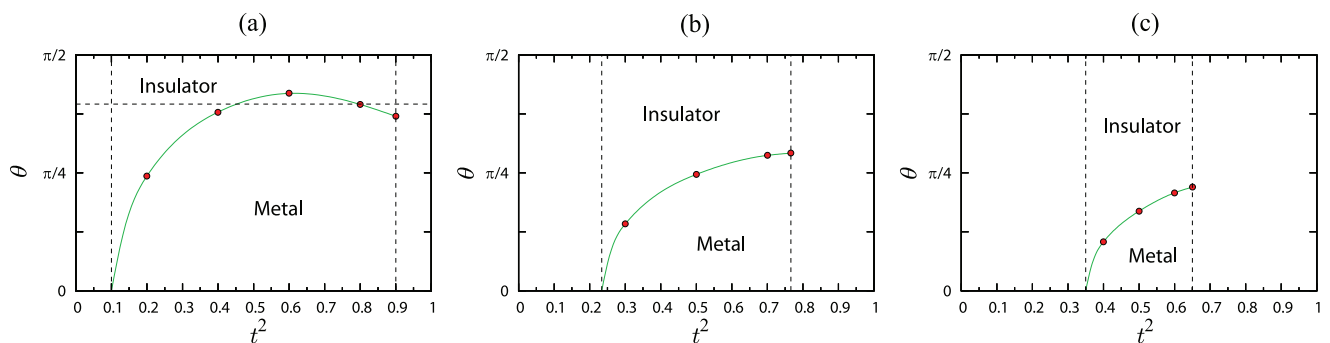


FIG. 17. (Color online) The phase diagrams obtained from the θ dependence of the normalized localization length Λ_{\parallel} on the two-dimensional cuts (a) I ($\delta^2 = 0.1$), (b) II ($\delta^2 = 0.234$), and (c) III ($\delta^2 = 0.35$). The critical points obtained by the finite-size scaling analysis are marked by red dots. The connecting green lines are guides to the eyes. The point $t^2 = \delta^2$ and $\theta = 0$ is critical by construction. The two vertical dashed lines in each panel indicate the allowed minimum and maximum values of t^2 . The horizontal dashed line in panel (a) represents the one-dimensional cut ‘‘F’’ ($\theta = 19\pi/48$) defined in Eq. (3.27).

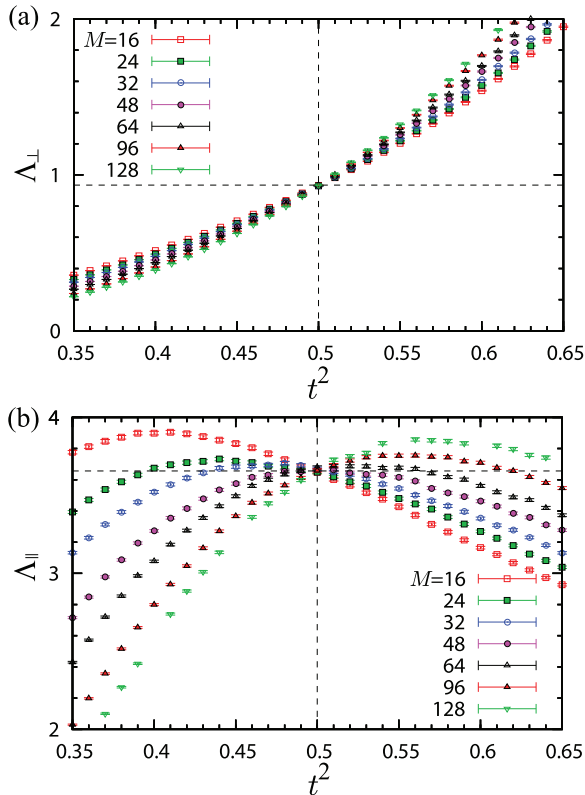


FIG. 18. (Color online) The t^2 dependence of the normalized localization lengths Λ_{\perp} in panel (a) and Λ_{\parallel} in panel (b) of the two-dimensional spin-directed \mathbb{Z}_2 network model with dimerization along the one-dimensional cut (3.26) at $\theta = \pi/4$ and $\delta^2 = 0.234$ for fixed M ranging from 16 to 128. The vertical and horizontal dashed lines represent t_c^2 and $\Lambda_{x,c}$ as deduced from the finite-size scaling analysis summarized in Table I, respectively.

$t^2 = 1 - \delta^2$ for a window of values of θ 's not too large. This metallic phase undergoes the transition to the insulating phase upon increasing θ . We also observe the reentrance driven by t^2 near $\theta \approx 3\pi/8$ on the two-dimensional cut (3.25a) in Fig. 17(a). The lower upper bound on the allowed values of t^2 resulting from the larger fixed values for δ^2 preempts any reentrance driven by t^2 for the two-dimensional cuts II and III in Figs. 17(b) and 17(c), respectively.

F. Dependence of the normalized localization length on t^2

We continue exploring the phase diagram 12(c) by studying the t^2 dependence of the normalized localization lengths Λ_{\perp} and Λ_{\parallel} .

1. Finite-size scaling for the normalized localization length with dimerization

To begin with, we consider the one-dimensional cut

$$E: (t^2, \pi/4, 0.234), \quad t^2 \in [0.234, 0.766] \quad (3.26)$$

of the three-dimensional parameter space (2.7). Cut E is shown in Fig. 14 with the label ‘‘E.’’ We note that this one-dimensional cut also contains the critical point $(0.5, \pi/4, 0.234)$ in Eq. (3.19). Figures 18(a) and 18(b) show the normalized localization lengths Λ_{\perp} and Λ_{\parallel} , respectively,

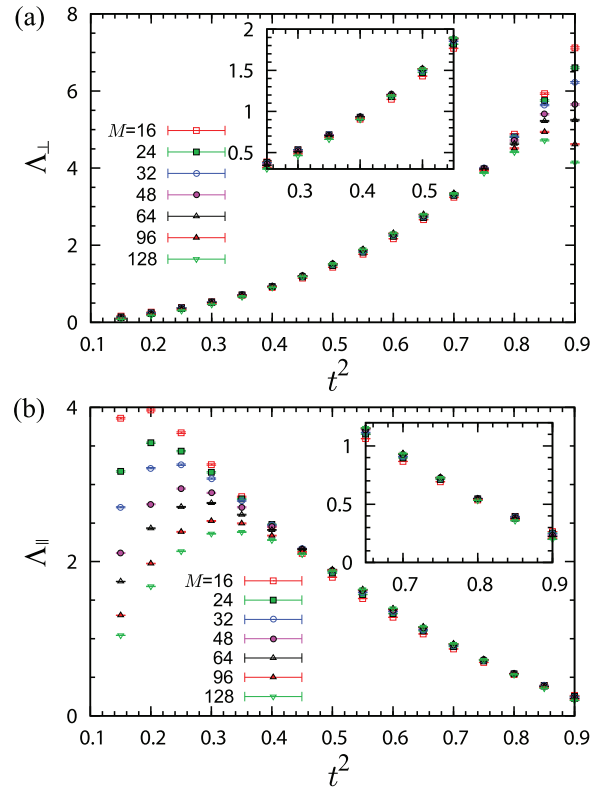


FIG. 19. (Color online) The t^2 dependence of the normalized localization lengths Λ_{\perp} in panel (a) and Λ_{\parallel} in panel (b) of the two-dimensional spin-directed \mathbb{Z}_2 network model with dimerization along the one-dimensional cut (3.27) at $\theta = 19\pi/48$ and $\delta^2 = 0.1$ for fixed M ranging from 16 to 128. Inset: Dependence on t^2 near $t^2 \approx 0.4$ for panel (a) and near $t^2 \approx 0.8$ for panel (b).

as a function of t^2 along the cut (3.26). The dependence of Λ_{\perp} and Λ_{\parallel} in Fig. 18 on the width M is reversed compared to the one displayed in Fig. 16. This is so because increasing t^2 along the cut E in Fig. 14 drives a transition from the insulating to the metallic phase, while increasing θ along the cut D in Fig. 14 drives a transition from the metallic to the insulating phase. We also note for Fig. 18(b) that, when the width M is sufficiently small, the normalized localization length Λ_{\parallel} for $t^2 < 0.5$ is larger than that for $t^2 > 0.5$, while this relation is inverted when M is sufficiently large. This observation is a manifestation of finite-size corrections to scaling.

In Fig. 17(a), we have observed reentrance near $\theta \approx 3\pi/8$ in the t^2 dependence of the normalized localization lengths Λ_{\perp} and Λ_{\parallel} . To examine in more detail reentrance driven by t^2 , we choose the one-dimensional cut

$$F: (t^2, 19\pi/48, 0.1), \quad t^2 \in [0.1, 0.9] \quad (3.27)$$

of the three-dimensional parameter space (2.7). Cut F is shown in Fig. 14 with the label ‘‘F.’’ Cut F is also shown in Fig. 17(a) by the horizontal dashed line.

Figures 19(a) and 19(b) show the normalized localization lengths Λ_{\perp} and Λ_{\parallel} , respectively, along the cut (3.27). Inspection of Fig. 17(a) shows that cut F comes close to an extended segment of the boundary between the metallic and insulating phases when $0.45 \leq t^2 \leq 0.8$. Hence, the proximity

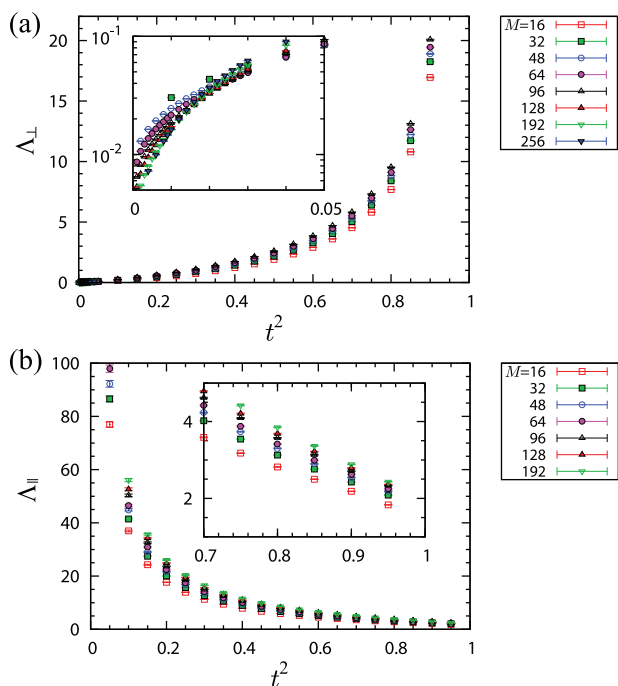


FIG. 20. (Color online) The t^2 dependence of the normalized localization lengths Λ_{\perp} in panel (a) and Λ_{\parallel} in panel (b) of the two-dimensional spin-directed \mathbb{Z}_2 network model without dimerization, at $\theta = \pi/4$, and for fixed M ranging from 16 to 256. Inset: Dependence on t^2 near $t^2 = 0$ for panel (a) and near $t^2 = 1$ for panel (b).

to the phase boundary of cut F when $0.45 \leq t^2 \leq 0.8$ implies that the dependence of the normalized localization lengths on the width M is weak along this portion of cut F in Fig. 14. Nevertheless, the signature of a metal-to-insulator transition upon increasing t^2 through $t^2 \approx 0.75$ and the signature of an insulator-to-metal transition upon increasing t^2 through $t^2 \approx 0.45$ are visible in Fig. 19(a) and in its inset, respectively. Reentrance is also visible in Fig. 19(b) and in its inset. We have also studied the normalized localization lengths along other one-dimensional cuts parametrized by t^2 in the planes I, II, and III defined by Eqs. (3.25a), (3.25b), and (3.25c), respectively. We have opted not to present these results for lack of space. It suffices to say that the dependence on t^2 along these cuts is compatible with the phase diagram in Fig. 17.

2. Finite-size scaling for the normalized localization length without dimerization

We continue by studying surface states of a weak three-dimensional \mathbb{Z}_2 topological insulator without dimerization, i.e., $\delta^2 = 0$ and we fix θ to the value $\pi/4$. This defines the one-dimensional cut

$$G: (t^2, \pi/4, 0), \quad t^2 \in [0, 1] \quad (3.28)$$

of the three-dimensional parameter space (2.7). Cut G is shown in Fig. 14 with the label ‘‘G.’’ The dependence on M of the normalized localization length Λ_{\perp} and Λ_{\parallel} corresponding to the geometries of Figs. 13(a) and 13(b), respectively, as t^2 is increased along the interval $[0, 1]$ is the following.

Figure 20 shows the normalized localization length Λ_{\perp} in panel (a) and Λ_{\parallel} in panel (b) as a function of t^2 . On the one

hand, according to Fig. 20(b), Λ_{\parallel} increases with increasing M for values of t^2 ranging from 0.05 to 0.95. This would be the signature for a metallic phase for these values of t^2 if we could show that Λ_{\perp} also diverges in the limit $M \rightarrow \infty$. According to Fig. 20(a), Λ_{\perp} also increases with increasing M for t^2 larger than 0.05. We conclude that the phase at $\delta^2 = 0$, $\theta = \pi/4$, and for $0.05 < t^2 < 0.95$ is metallic.

For values of t^2 smaller than 0.05, Λ_{\perp} decreases with increasing M very close to $t^2 = 0$ according to the inset of Fig. 20(a). However, this apparent insulating dependence on M of Λ_{\perp} for $t^2 < 0.05$ might be a finite-size artifact due to the fact that Λ_{\perp} must vanish at $t^2 = 0$. In this scenario, the value of M beyond which metallic dependence of Λ_{\perp} on M is the rule diverges as $t^2 \rightarrow 0$. This scenario is consistent with the observation that the goodness of fit \mathcal{G} in Eq. (3.16) is the poorest for $t^2 < 0.05$. Moreover, the following argument supports this scenario and the conclusion that the phase is metallic inside the two-dimensional cut of parameter space at $\delta^2 = 0$.

When $t^2 = 0$, the two-dimensional spin-directed \mathbb{Z}_2 network model realizes a unidirectional metal that consists of M (even) independent pairs of helical edge states supporting the dimensionless conductance M along their direction of propagation [the direction \parallel in the geometry of Fig. 20(b)] and a vanishing conductance in the orthogonal direction [the direction \perp in the geometry of Fig. 20(a)]. We first assume that $\lim_{M \rightarrow \infty} \Lambda_{\perp} = 0$, where the limit $M \rightarrow \infty$ is taken with M even, persists away from $t^2 = 0$ for sufficiently small values of t^2 . We are going to show that this first assumption contradicts the second assumption $\lim_{M \rightarrow \infty} \Lambda_{\parallel} = \infty$, where the limit $M \rightarrow \infty$ is taken with M even, for all values of t^2 . [The second assumption is supported empirically for all the values of t^2 shown in Fig. 20(b), whereas the first assumption is not unambiguously supported by Fig. 20(a).] These two assumptions are in mutual contradiction, for the first assumption implies that the two-dimensional spin-directed \mathbb{Z}_2 network model realizes a quasi-one-dimensional quantum wire with an even number $2M$ of channels in the symplectic symmetry class. Such a quasi-one-dimensional wire is necessarily localized, i.e., $\lim_{M \rightarrow \infty} \Lambda_{\parallel} = 0$, in contradiction with the second assumption. Since our finite-size scaling analysis puts the second assumption on firmer ground than the first assumption, we conclude that a two-dimensional metallic phase in the symplectic symmetry class is established for any nonvanishing t^2 .

G. Dependence of the normalized localization length on $\delta\phi$

So far, we have focused on the maximally disordered case by setting $\delta\phi = 2\pi$ in Eq. (2.7). It is time to investigate how the normalized localization lengths Λ_{\perp} and Λ_{\parallel} at the point (3.19) marked by the triangle in Fig. 14 depend on the width $\delta\phi$ of the random phases defined in Eq. (2.6). We recall that the triangle in Fig. 14 is the critical point defined by the intersection of the cuts A, D, and E when $\delta\phi = 2\pi$.

The dependence on $0 \leq \delta\phi \leq 2\pi$ of the normalized localization lengths Λ_{\perp} and Λ_{\parallel} , respectively, at the point (3.19) is shown in Figs. 21(a) and 21(b). We observe that Λ_{\perp} and Λ_{\parallel} are both increasing functions of $0 \leq \delta\phi < 2\pi$ that appear to converge to the critical values of Λ_{\perp}^c and Λ_{\parallel}^c , respectively, at the critical point (3.19) when $\delta\phi = 2\pi$. Hence, disorder favors delocalization over localization for the surface states of weak

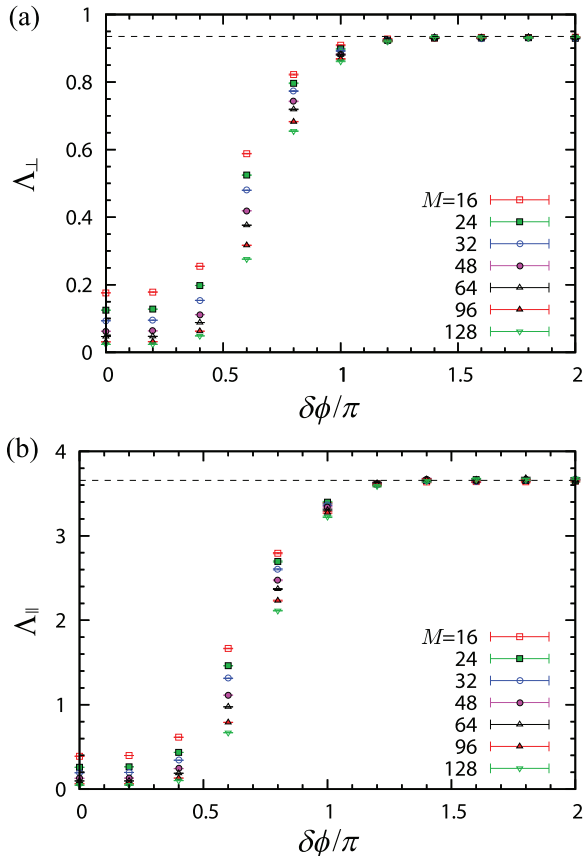


FIG. 21. (Color online) The $\delta\phi$ dependence of the normalized localization lengths Λ_{\perp} in panel (a) and Λ_{\parallel} in panel (b) of the two-dimensional spin-directed \mathbb{Z}_2 network model at $t^2 = 0.5$, $\theta = \pi/4$, and $\delta^2 = 0.234$ for fixed M ranging from 16 to 128. The horizontal dashed lines in panels (a) and (b) represent $\Lambda_{\perp}^c = 0.935$ and $\Lambda_{\parallel}^c = 3.657$, respectively.

three-dimensional \mathbb{Z}_2 topological insulators. For any fixed $0 \leq \delta\phi < 2\pi$, we also observe that the normalized localization lengths Λ_{\perp} and Λ_{\parallel} both decrease with increasing the width M . This insulating behavior is caused by the finite dimerization $\delta^2 = 0.23$. Hence, we deduce that the cut

$$H: (t^2, \theta, \delta\phi, \delta^2) := (0.5, \pi/4, \delta\phi, 0.23), \quad 0 \leq \delta\phi < 2\pi \quad (3.29)$$

realizes an insulating phase. Along the same lines, we expect that the phase diagrams presented in Fig. 17 are qualitatively correct for a weaker disorder $0 < \delta\phi < 2\pi$ than $\delta\phi = 2\pi$, albeit with a smaller metallic region.

IV. NUMERICAL DATA FOR AN ODD NUMBER OF DIMERIZED CHANNELS

As was emphasized in Refs. [40,60,61], weak three-dimensional \mathbb{Z}_2 topological insulators are characterized by a dependence on the parity in the stacking number of strong two-dimensional \mathbb{Z}_2 topological insulators. This parity effect can be illustrated in the context of the two-dimensional spin-directed \mathbb{Z}_2 network model by weakly perturbing the quasi-one-dimensional symplectic metallic fixed point (2.9) from Sec. II C 1 in the limit M fixed and $L \rightarrow \infty$. In this

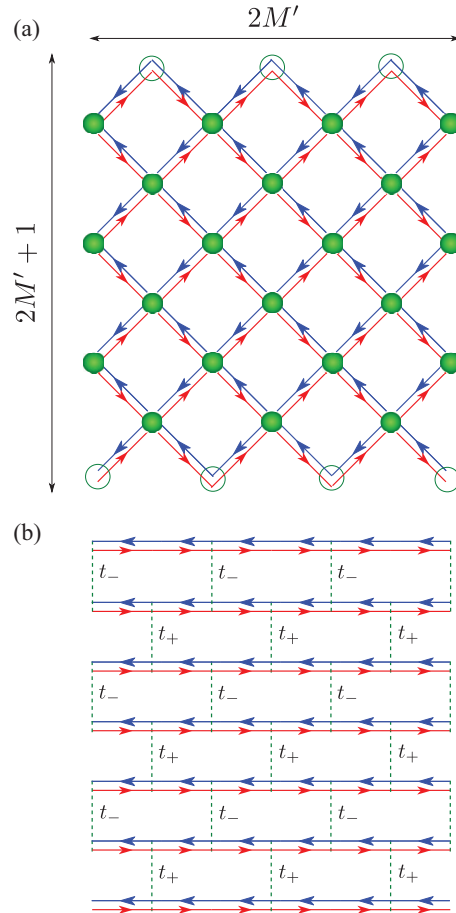


FIG. 22. (Color online) A two-dimensional spin-directed \mathbb{Z}_2 network model with the dimensions $(2M' + 1) \times 2M'$ where $M' = 3$ in the vertex (a) and the brick-wall representations (b), respectively. The difference with the two-dimensional spin-directed \mathbb{Z}_2 network model shown in Fig. 6(a) is the addition of a bottom and a top row of vertices represented by empty circles at which perfectly reflecting boundary conditions must be imposed in panel (a).

quasi-one-dimensional limit, the localization properties of the two-dimensional spin-directed \mathbb{Z}_2 network model depend on the parity of M . If $M = 2M'$ is even, as we have assumed all along so far, then the transfer matrix belongs to the Lie group $SO^*(4M')$ and exponential localization is the rule [62]. If $M = 2M' + 1$ is odd, the transfer matrix belongs to the Lie group $SO^*(4M' + 2)$ and there is one pair of Kramers degenerate helical quasi-one-dimensional channels that is perfectly conducting [6–8].

We are going to derive this parity effect for the two-dimensional spin-directed \mathbb{Z}_2 network model shown in Fig. 22 that represents surface states from stacked layers of an odd number of strong two-dimensional \mathbb{Z}_2 topological insulators in Fig. 2. By comparing Fig. 6(a) with Fig. 22(a), we observe that two rows of vertices denoted by empty circles were added in Fig. 22(a) at the bottom and at the top of Fig. 6(a). Correspondingly, all vertices represented by filled circles colored in green in Fig. 22(a) correspond to the elementary scattering process between four incoming and four outgoing plane waves defined in Eq. (2.3), while all vertices represented by empty circles in Fig. 22(a) correspond to the perfectly

reflecting boundary condition

$$\begin{pmatrix} \psi_{\uparrow}^{(o)} \\ \psi_{\downarrow}^{(o)} \end{pmatrix} = S_{\text{ref}} \begin{pmatrix} \psi_{\uparrow}^{(i)} \\ \psi_{\downarrow}^{(i)} \end{pmatrix}, \quad S_{\text{ref}} := e^{i\phi} \sigma_0, \quad (4.1)$$

where $0 \leq \phi \leq 2\pi$ [Fig. 22(a)].

The total transfer matrix $\mathcal{M}_{\parallel, \text{tot}}$ that defines a two-dimensional spin-directed \mathbb{Z}_2 network model with $2M' + 1$ Kramers' pairs of conducting channels is built from the elementary 4×4 transfer matrix \mathcal{M}_{\parallel} defined in Eq. (3.2b) and the elementary 2×2 transfer matrix defined by

$$\begin{pmatrix} \psi_{\uparrow}^{(o)} \\ \psi_{\downarrow}^{(i)} \end{pmatrix} = \mathcal{M}_{\text{ref}} \begin{pmatrix} \psi_{\uparrow}^{(i)} \\ \psi_{\downarrow}^{(o)} \end{pmatrix}, \quad \mathcal{M}_{\text{ref}} := \begin{pmatrix} e^{+i\phi} & 0 \\ 0 & e^{-i\phi} \end{pmatrix}. \quad (4.2)$$

The matrix $\mathcal{M}_{\parallel, \text{tot}}$ belongs to the Lie group $\text{SO}^*(4M' + 2)$.

Hence, the matrix $\mathcal{M}_{\parallel, \text{tot}}^{\dagger} \mathcal{M}_{\parallel, \text{tot}}$ has doubly degenerate eigenvalues of the form $\exp(\pm 2X_{\parallel, j})$ with $j = 1, \dots, M/2$ as well as doubly degenerate eigenvalues of the form $\exp(2X_{\parallel, 0}) = 1$, i.e., $X_{\parallel, 0} = 0$. We shall assume the convention

$$0 = X_{\parallel, 0} < X_{\parallel, 1} < \dots < X_{\parallel, M/2} \quad (4.3)$$

when ordering the Lyapunov exponents.

We have computed numerically the Lyapunov exponents $X_{\parallel, j}$ by the transfer matrix method [55]. In the quasi-one-dimensional limit, as anticipated, we have found the doubly degenerate eigenvalues $X_{\parallel, 0} = 0$ for a sampling of points from the three-dimensional parameter space (2.7). Since the largest localization length is nothing but the inverse of the Lyapunov exponent $X_{\parallel, 0}$, the fact $X_{\parallel, 0} = 0$ is interpreted as the existence of a perfectly conducting pair of Kramers' degenerate quasi-one-dimensional channels associated to an infinite localization length anywhere in the three-dimensional parameter space (2.7). In other words, stacking an odd number of strong two-dimensional \mathbb{Z}_2 topological insulators in Fig. 2 always delivers a single perfectly conducting pair of Kramers' degenerate quasi-one-dimensional channels for arbitrary dimerization and arbitrary local disorder that preserve time-reversal symmetry. The same result was also obtained in Ref. [40]. This implies that, even in the insulating phase in the phase diagram of Fig. 12, there exists a single pair of Kramers' degenerate quasi-one-dimensional channels of perfect conduction as long as M is odd. Hereby, surface states of a weak three-dimensional \mathbb{Z}_2 topological insulator with an odd number of stacking layers support, in the quasi-one-dimensional limit, a perfectly conducting pair of Kramers' degenerate quasi-one-dimensional channels, even in the presence of dimerizations.

We have also applied the finite-size scaling analysis encoded by Eqs. (3.4) and (3.5) to the normalized localization length Λ_{\parallel} obtained from the *second* smallest Lyapunov exponent $X_{\parallel, 1}$. The δ^2 dependence of the normalized localization length Λ_{\parallel} along the one-dimensional cut ‘‘A’’ defined in Eq. (3.17) for various width M is summarized in Fig. 23. Although finite-size corrections are more pronounced for an odd stacking than for an even stacking in Fig. 2, the first subleading normalized localization length Λ_{\parallel} undergoes a metal-insulator transition at $\delta_c^2 \approx 0.234$ belonging to the same universality class as that occurring for an even stacking. This

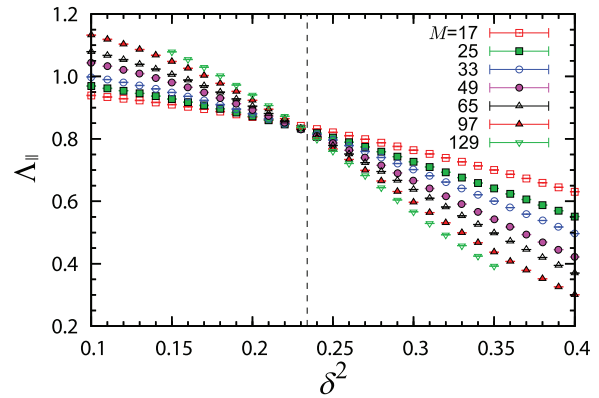


FIG. 23. (Color online) The δ^2 dependence of the normalized localization length Λ_{\parallel} calculated from the second smallest positive Lyapunov exponent $X_{\parallel, 1}$ for the spin-directed \mathbb{Z}_2 network model with an odd number channels. The parameter t^2 and θ are fixed to $t^2 = 0.5$ and $\theta = \pi/4$, so as to facilitate comparison with Fig. 15 when the number of channels is even, while all other parameters are the same. The vertical dashed line represents $\delta_c^2 = 0.234$, as deduced from the finite-size scaling analysis summarized in Table I.

suggests that a ‘‘two-fluid picture’’ applies when stacking an odd number of strong two-dimensional \mathbb{Z}_2 topological insulators in Fig. 2 in the quasi-one-dimensional limit. While there exists a perfectly conducting quasi-one-dimensional channel, the localization properties of all remaining quasi-one-dimensional channels are those of an even number of stacked strong two-dimensional \mathbb{Z}_2 topological insulators in Fig. 2.

V. NUMERICAL DATA WITH TRIMERIZATION

The parity effect discussed in Sec. IV is also the reason for which the spin-directed \mathbb{Z}_2 network model with trimerization shown in Fig. 24 is always delivering a metallic phase. We first defend this assertion using a qualitative argument. We then present numerical results in support of this assertion.

A. Qualitative argument

In the limit of $t_+ \gg t_-$, we may replace the three pairs of helical modes in a trimer by a single effective pair of helical modes, which is then coupled by t_- to its neighboring effective pairs of helical modes. Thus, the two-dimensional trimerized spin-directed \mathbb{Z}_2 network model reduces to a two-dimensional spin-directed \mathbb{Z}_2 network model without polymerization in this limit. In the opposite limit $t_+ \ll t_-$, any two pairs of helical modes coupled by t_- become inert (localized) and the remaining pairs of helical modes are weakly coupled without polymerization. The same conclusion follows from the point of view of surface states realizing an even number of Dirac cones. Scattering matrix elements are needed that couple pairwise the surface Dirac cones in order to localize the Dirac modes. Trimerization does not deliver such matrix elements.

From the examples of dimerization and trimerization, we conjecture the following parity effect. The combined effects of polymerization and disorder for the two-dimensional spin-directed \mathbb{Z}_2 network model produces a phase diagram with either (i) two insulating phases separated by a metallic phase when the breaking of translation symmetry involves a repeat unit cell consisting of an even number of helical modes in the

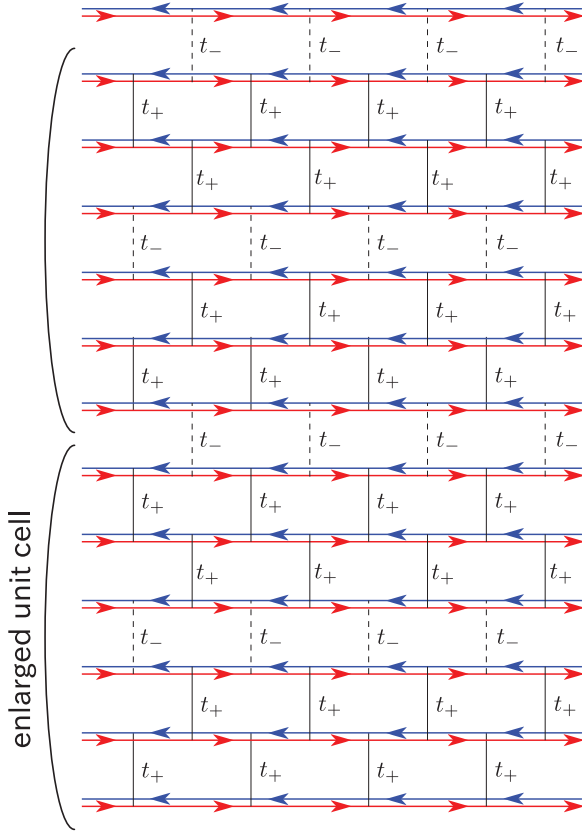


FIG. 24. (Color online) Two-dimensional spin-directed \mathbb{Z}_2 network model with $M = 6M'$ an even integer multiple of 3. The periodic pattern for the transmission amplitudes implements a trimerization, as is indicated by the enlarged unit cell.

clean limit, (ii) or a single metallic phase when the breaking of translation symmetry involves a repeat unit cell consisting of an odd number of helical modes in the clean limit.

B. Numerics

1. Transfer matrix

Two transfer matrices \mathcal{M}_\perp and \mathcal{M}_\parallel are defined as in Sec. III A, except for the pattern of trimerization shown in Fig. 24 for the transmission amplitude.

2. Definition of the normalized localization length

The normalized localization lengths Λ_\perp and Λ_\parallel are defined as in Sec. III B, except for the pattern of trimerization shown in Fig. 24 for the transmission amplitude.

3. Finite-size scaling for the normalized localization length in the presence of trimerization

Figure 25 shows the δ^2 dependence of the normalized localization lengths Λ_\perp and Λ_\parallel along the one-dimensional cut (3.17) with $t_\pm^2 = 0.5 \pm \delta^2$ and $\theta = \pi/4$ in the two-dimensional trimerized spin-directed \mathbb{Z}_2 network model.

According to Fig. 25(a), the normalized localization length Λ_\perp at fixed $t_\pm^2 = 0.5 \pm \delta^2$, $\theta = \pi/4$, and δ^2 increases with increasing M , whereas it is a decreasing function with increasing δ^2 at fixed $t_\pm^2 = 0.5 \pm \delta^2$, $\theta = \pi/4$, and M . The latter decrease of Λ_\perp with increasing δ^2 is expected since

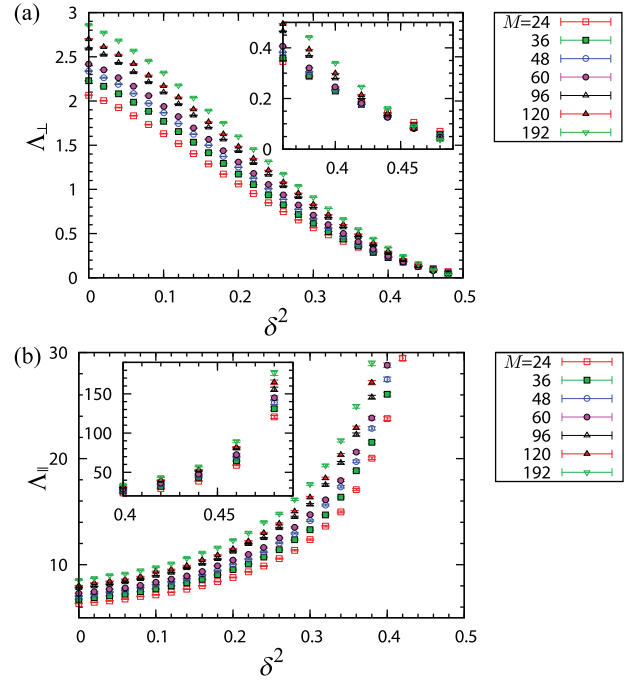


FIG. 25. (Color online) Combined effects of trimerization and disorder for a two-dimensional spin-directed \mathbb{Z}_2 network model. The δ^2 dependence of the normalized localization length at $t^2 = 0.5$ and $\theta = \pi/4$ for fixed M ranging from 24 to 192 is shown in panel (a) for Λ_\perp and in panel (b) for Λ_\parallel . Inset: Dependence on δ^2 near $\delta^2 = 0.5$ for panel (a) and for panel (b).

$\Lambda_\perp = 0$ because of $t_-^2 = 0$ at $\delta^2 = 0.5$. A signature of the point $t_-^2 = 0$ is visible in the inset of Fig. 25(a) in which the dependence of Λ_\perp on $0.25 < \delta^2 < 0.5$ for fixed M ranging from 24 to 192 is shown. Indeed, upon approaching from below $\delta^2 = 0.5$, the dependence of Λ_\perp on M undergoes a crossover from monotonically increasing to monotonically decreasing. We attribute this fact to the same finite-size artifact discussed in the last paragraph of Sec. III F 2 that is responsible for a similar crossover of Λ_\perp on M in the inset of Fig. 20(a) upon approaching from above $t^2 = 0$.

According to Fig. 25(b), the normalized localization length Λ_\parallel at fixed $t_\pm^2 = 0.5 \pm \delta^2$, $\theta = \pi/4$, and δ^2 increases with increasing M . Moreover, it is an increasing function of δ^2 at fixed $t_\pm^2 = 0.5 \pm \delta^2$, $\theta = \pi/4$, and M .

Thus, there is no sign of a transition from a metallic to an insulating phase in the two-dimensional trimerized spin-directed \mathbb{Z}_2 network model upon increasing the value of δ^2 , as was the case for the two-dimensional dimerized spin-directed \mathbb{Z}_2 network model at the critical point (3.19) (see Fig. 15). The absence of the insulating phase in the two-dimensional spin-directed \mathbb{Z}_2 network model with trimerizations has also been confirmed by studying the θ and t^2 dependencies along the cuts (3.23) and (3.26), respectively, of the normalized localization lengths Λ_\perp and Λ_\parallel .

VI. SUMMARY AND DISCUSSION

We have shown that the surface states of a weak three-dimensional \mathbb{Z}_2 topological insulator can be modeled by a

two-dimensional spin-directed \mathbb{Z}_2 network model. In other words, a two-dimensional spin-directed \mathbb{Z}_2 network model can be interpreted as an effective lattice regularization for the surface states of a weak three-dimensional \mathbb{Z}_2 topological insulator. The qualifier \mathbb{Z}_2 indicates here that time-reversal symmetry is present, but $SU(2)$ spin-rotation symmetry is broken.

We have studied the combined effects of polymerization and disorder in a two-dimensional spin-directed \mathbb{Z}_2 network model. Polymerization implies that the lattice symmetry group \mathcal{G} of the two-dimensional spin-directed \mathbb{Z}_2 network model is reduced to a nontrivial subgroup \mathcal{G}' in the clean limit.

On the one hand, if the polymerization opens a spectral gap in the clean limit and if the disorder strength is weak relative to the polymerization gap, single-particle states are localized. As the ratio of the disorder strength to the polymerization gap is increased, a quantum phase transition from an insulating to a metallic phase takes place. This transition is smooth and we have shown that it belongs to the two-dimensional symplectic universality class in the theory of Anderson localization, as measured by the power-law divergence of the localization length with the scaling exponent $\nu \approx 2.7$. This metallic phase is connected to the critical point that separates the two polymerized-gapped phases in the clean limit.

On the other hand, if the polymerization does not open a spectral gap in the clean limit, i.e., if the pattern of symmetry breaking $\mathcal{G} \rightarrow \mathcal{G}'$ is associated to an enlarged unit cell of the two-dimensional spin-directed \mathbb{Z}_2 network model that is built out of an odd integer number of the unit cell prior to switching on polymerization, then the metallic phase is robust to any short-range correlated disorder.

The two-dimensional spin-directed \mathbb{Z}_2 network model studied in this paper is the second example of a two-dimensional directed network model after that of the directed CC network model. Similarly to the directed CC network model, it is an effective lattice model that captures some low-energy and long-wavelength properties of surface states of weak three-dimensional topological insulators, such as the universal properties of a quantum phase transition from the theory of Anderson localization. There is an important difference with regard to the long-distance physics of the two classes of network models, however. Charge transport for the directed CC network model is intrinsically anisotropic: ballistic chiral transport in one direction and critical (diffusive) transport in the other direction. By contrast, charge transport for the spin-directed \mathbb{Z}_2 network model is effectively isotropic at long wavelengths, as is illustrated after a rescaling of velocities in the limiting Dirac Hamiltonians.

There exists a network model for each of the 10 symmetry classes in the theory of Anderson localization [63]. Regardless of the dimensionality of space, five of these network models encode the effects of disorder on strong topological insulators, noninteracting insulators with response functions whose topological character is protected by symmetry [64–66]. By stacking and weakly coupling a family of strong two-dimensional topological insulators from a given symmetry class, one obtains a weak three-dimensional topological insulator. We conjecture that the combined effects of breaking the stacking symmetry in a periodic way (polymerization) and disorder on the phase diagram of a weak three-dimensional topological insulator from a given symmetry class are captured

by a two-dimensional “directed” network model built out of an elementary scattering matrix within this symmetry class. As we have seen for the two-dimensional spin-directed \mathbb{Z}_2 network model of this paper, and as expected from theoretical considerations [38,53,67–69], unpolymerized network models are not expected to support insulating phases. Furthermore, the dichotomy between anisotropic versus isotropic transport is expected to apply to the three symmetry classes with a \mathbb{Z} index (the symmetry classes A, C, and D) and the two symmetry classes with a \mathbb{Z}_2 index (the symmetry classes AII and CII), respectively [38].

An outstanding open problem is the interplay of disorder and interactions for the surface states of three-dimensional weak \mathbb{Z}_2 topological insulators, given the fact that interactions can stabilize states of matter that fall outside the classification of noninteracting topological insulators [67,70–82].

ACKNOWLEDGMENTS

We thank J. Bardarson for helpful discussions. S.R., A.F., and C.M. thank the KITP program Topological Insulators and Superconductors for hospitality where this work was initiated. H.O. was supported by Grants-in-Aid (Grants No. 25800213 and No. 25390113) from the Japan Society for Promotion of Science. The work of A.F. was partly supported by a Grant-in-Aid (Grant No. 24540338) from the Japan Society for Promotion of Science and by the RIKEN iTHES project.

APPENDIX A: QUASI-ONE-DIMENSIONAL MODEL FOR THE SURFACE STATES OF A WEAK THREE-DIMENSIONAL \mathbb{Z}_2 TOPOLOGICAL INSULATOR

Figure 1 depicts a two-dimensional \mathbb{Z}_2 topological *band* insulator. The interior of the ellipse shown in Fig. 1(a) is called the bulk. The boundary of the ellipse shown in Fig. 1(a) is the edge. Figure 1 represents a model of noninteracting electrons such that (i) the single-particle eigenstates with support in the bulk display a spectral gap Δ as is indicated in Fig. 1(b), while (ii) the single-particle eigenstates with support on the edge realize a twofold degenerate dispersion that crosses the spectral gap of the bulk states as is indicated in Fig. 1(b), are extended along the edge, but are exponentially localized in the direction perpendicular to the edge. These edge states represent a single pair of Kramers’ degenerate electrons propagating with opposite velocities. These edge states are also called helical states as the expectation values of the electronic spins are opposite for each electron forming the Kramers’ degenerate pair and change with the momenta k of the electrons parallel to the edge. The low-energy and long-wavelength effective Hamiltonian of the single pair of helical states depicted in Fig. 1(a) is

$$\hat{H}_{\text{Helical}} := \int_{\text{edge}} dx (\hat{\Psi}^\dagger(-i)v\sigma_3\partial_x\hat{\Psi})(x). \quad (\text{A1a})$$

Units are chosen so that $\hbar = 1$. The speed v is positive by convention. The operators $\hat{\Psi}_\alpha^\dagger(x)$ and $\hat{\Psi}_\alpha(x)$ create and destroy at the position x along the edge an electron with the projection $\alpha = \uparrow, \downarrow$ of its spin along the spin quantization axis, respectively. They make up the doublet of operators $\hat{\Psi}^\dagger(x)$ and $\hat{\Psi}(x)$, respectively. The Pauli matrices σ_1, σ_2 , and σ_3 act on

the spin components of the electrons. The unit 2×2 matrix in spin space is denoted σ_0 . Hamiltonian (A1a) is invariant under the operation of time reversal defined by

$$\hat{\Psi}^\dagger(x) = \hat{\Psi}^\dagger(x) K \sigma_2, \quad \hat{\Psi}(x) = \sigma_2 K \hat{\Psi}'(x), \quad (\text{A1b})$$

$$\begin{aligned} \hat{H}_{\text{layered}} := & \int_{\text{edge}} dx \sum_{n=1}^{2N} [(\hat{\Psi}_n^\dagger(-i) v_n \sigma_3 \partial_x \hat{\Psi}_n(x) + \hat{\Psi}_n^\dagger(x) \mu_n(x) \sigma_0 \hat{\Psi}_n(x)] \\ & + \int_{\text{edge}} dx \sum_{n=1}^{2N-1} \left[\hat{\Psi}_{n+1}^\dagger(x) \left(\frac{\lambda_{n,0}}{2} \sigma_0 + i \sum_{j=1}^3 \frac{\lambda_{n,j}}{2} \sigma_j \right) \hat{\Psi}_n(x) + \text{H.c.} \right]. \end{aligned} \quad (\text{A2a})$$

There is an even number of layers $2N$. Each layer n with $n = 1, \dots, 2N$ has its own Fermi velocity $v_n > 0$ and chemical potential $\mu_n \in \mathbb{R}$. Any two consecutive layers are coupled by hopping matrix elements parametrized by the four independent real-valued couplings $\lambda_{n,\mu}$ with $\mu = 0, 1, 2, 3$ and $n = 1, \dots, 2N - 1$. Open boundary conditions are chosen along the layering axis. Hamiltonian (A2a) is invariant under the operation of time reversal defined by

$$\hat{\Psi}_n^\dagger(x) = \hat{\Psi}_n^\dagger(x) K \sigma_2, \quad \hat{\Psi}_n(x) = \sigma_2 K \hat{\Psi}_n'(x), \quad (\text{A2b})$$

where K denotes the operation of complex conjugation and $n = 1, \dots, 2N$. Hamiltonian (A2a) is depicted in Fig. 2.

We can turn the layered model (A2) into a layered microscopic model of a weak three-dimensional \mathbb{Z}_2 topological band insulator by demanding that

$$\begin{aligned} v_n &= v_{u,x} + (-1)^n v_s, \quad \mu_n = \mu_u + (-1)^n \mu_s, \\ \lambda_{n,\mu} &= (1 - \delta_{n,2N}) [\lambda_{u,\mu} + (-1)^n \lambda_{s,\mu}], \quad \mu = 0, 1, 2, 3 \end{aligned} \quad (\text{A3})$$

for $n = 1, \dots, 2N$.

It is shown in the Supplemental Material [45] how to construct a continuum limit of \hat{H}_{layered} that delivers the single-particle Dirac Hamiltonian

$$\begin{aligned} \mathcal{H}_d^{\text{All}} \equiv & v_{s,x} \sigma_3 \otimes \tau_3 (-i) \partial_x + v_{u,y} \sigma_0 \otimes \tau_1 (-i) \partial_y \\ & + \bar{u}_{+,0} \sigma_0 \otimes \tau_0 + \bar{u}_{-,0} \sigma_0 \otimes \tau_3 \\ & + \sum_{j=1}^3 2 \bar{w}_{+,j}'' \sigma_j \otimes \tau_1 + 2 \bar{w}'_{-,0} \sigma_0 \otimes \tau_2. \end{aligned} \quad (\text{A4})$$

The parameters $v_{s,x}$ and $v_{u,y}$ enter as anisotropic Dirac velocities. The parameter $\bar{u}_{+,0}$ enters as a chemical potential. The parameter $2 \bar{w}'_{-,0}$ enters as a mass. The mass term anticommutes with all terms except for the chemical potential. The remaining four terms with the parameters $\bar{u}_{-,0}$ and $\bar{w}_{+,j}''$ ($j = 1, 2, 3$) do not anticommute with all the gamma matrices multiplying the first derivatives in position space.

APPENDIX B: DIRAC HAMILTONIAN FROM THE TWO-DIMENSIONAL SPIN-DIRECTED \mathbb{Z}_2 NETWORK MODEL

Starting from the two-dimensional CC network model, Ho and Chalker derived in Ref. [83] the random Dirac Hamiltonian studied in Ref. [84] on its own merits. The two-dimensional \mathbb{Z}_2

where K denotes the operation of complex conjugation.

A layered microscopic model that captures the tunneling of helical edge states between adjacent layers for energy scales below the bulk gap Δ is defined by the Hamiltonian

network model for a strong two-dimensional \mathbb{Z}_2 topological insulator was related to a random Dirac Hamiltonian in Ref. [44]. As we show in the Supplemental Material, it is possible to take the continuum limit of the two-dimensional spin-directed \mathbb{Z}_2 network model by performing a gradient expansion of the random phases entering the network model and by performing an expansion in the deviations about the points

$$(t^2, \theta, \delta^2) = (t^2, \pi/2, 0) \quad (\text{B1})$$

and

$$(t^2, \theta, \delta^2) = (t^2, 0, 0), \quad (\text{B2})$$

respectively, in the three-dimensional parameter space (2.7).

As derived in the Supplemental Material [45], close to the point (B1), the continuum limit of the two-dimensional spin-directed \mathbb{Z}_2 network model is captured by the single-particle Dirac Hamiltonian

$$\begin{aligned} \mathcal{H}_{\theta=\pi/2} = & [t r(p_x - p_y) \sigma_1 + (r^2 p_x + t^2 p_y) \sigma_2] \otimes \tau_0 \\ & - [t r(A_x - A_y) \sigma_1 + (r^2 A_x + t^2 A_y) \sigma_2] \otimes \tau_3 \\ & - m \sigma_3 \otimes \tau_3 + V_0 \sigma_0 \otimes \tau_0 \\ & - \theta' t (\lambda_\phi \sigma_0 \otimes \tau_1 + 2 \sigma_0 \otimes \tau_2). \end{aligned} \quad (\text{B3a})$$

Here, a second set of Pauli matrices τ_1 , τ_2 , and τ_3 , together with the unit 2×2 matrix τ_0 , has been introduced. There appear the two-dimensional momentum operators p_x and p_y and a mass m . This Hamiltonian is invariant under reversal of time, i.e.,

$$\mathcal{T} \mathcal{H}_{\theta=\pi/2} \mathcal{T}^{-1} = \mathcal{H}_{\theta=\pi/2}, \quad \mathcal{T} := i \sigma_2 \otimes \tau_1 K, \quad (\text{B3b})$$

where K denotes the operation of complex conjugation. The mass m that encodes the dimerization ($m \propto \delta^2$) multiplies the matrix $\sigma_3 \otimes \tau_3$ that anticommutes with all other contributions to the continuum limit (B3a) with $V_0 = 0$. Hence, dimerization opens a spectral gap in the spectrum of Hamiltonian (B3a). The other parameters A_x , A_y , V_0 , λ_ϕ , and $\theta' \equiv \pi/2 - \theta$ commute with all other terms, except for the term with m . At the isotropic point defined by $t^2 = r^2 = \frac{1}{2}$, Hamiltonian (B3a) becomes the Dirac Hamiltonian

$$\begin{aligned} \mathcal{H}_{\theta=\pi/2} = & \frac{1}{\sqrt{2}} (p'_x \sigma_1 + p'_y \sigma_2) \otimes \tau_0 + V_0 \sigma_0 \otimes \tau_0 \\ & - \frac{1}{\sqrt{2}} (A'_x \sigma_1 + A'_y \sigma_2) \otimes \tau_3 - m \sigma_3 \otimes \tau_3 \\ & - \frac{\theta'}{\sqrt{2}} (\lambda_\phi \sigma_0 \otimes \tau_1 + 2 \sigma_0 \otimes \tau_2) \end{aligned} \quad (\text{B4a})$$

where

$$\begin{aligned} p'_x &\equiv \frac{p_x - p_y}{\sqrt{2}}, & p'_y &\equiv \frac{p_x + p_y}{\sqrt{2}}, \\ A'_x &\equiv \frac{A_x - A_y}{\sqrt{2}}, & A'_y &\equiv \frac{A_x + A_y}{\sqrt{2}}. \end{aligned} \quad (\text{B4b})$$

Close to the point (B2), the continuum limit of the two-dimensional spin-directed \mathbb{Z}_2 network model is captured by the single-particle Dirac-like Hamiltonian

$$\begin{aligned} \mathcal{H}_{\theta=0} &= p_x \sigma_0 \otimes \tau_3 + (tr p_y \sigma_1 + t^2 p_y \sigma_2) \otimes \tau_0 \\ &+ [tr(A_x - A_y)\sigma_1 - (r^2 A_x + t^2 A_y)\sigma_2] \otimes \tau_3 \\ &+ m \sigma_3 \otimes \tau_3 + \theta t (\lambda_\phi \sigma_0 \otimes \tau_1 + 2 \sigma_0 \otimes \tau_2) \\ &+ V_0 \sigma_0 \otimes \tau_0. \end{aligned} \quad (\text{B5a})$$

This Hamiltonian is invariant under reversal of time, i.e.,

$$\mathcal{T} \mathcal{H}_{\theta=0} \mathcal{T}^{-1} = \mathcal{H}_{\theta=0}, \quad \mathcal{T} := i \sigma_2 \otimes \tau_1 K, \quad (\text{B5b})$$

where K denotes the operation of complex conjugation. As was the case for the continuum limit (B3a), the term $V_0 \sigma_0 \otimes \tau_0$ acts as a chemical potential, for it commutes with all contributions to the continuum limit (B5a). We shall set $V_0 = 0$ when deciding if a gap at energy 0 is opened by

dimerization. In comparison to the continuum limit (B3a), the term $p_x \sigma_0 \otimes \tau_3$ has appeared that commutes with all contributions to the continuum limit (B5a) except for the term $\theta t (\lambda_\phi \sigma_0 \otimes \tau_1 + 2 \sigma_0 \otimes \tau_2)$. If we set $t = A_x = A_y = V_0 = 0$, we find the two (twofold degenerate) gapless dispersions $|p_x \pm m|$. More generally, a branch of excitation is expected to cross the energy 0 at some m -dependent value of the momentum when $\theta = V_0 = 0$. As the coupling m is caused by dimerization, dimerization thus fails to open a gap if we set $\theta = V_0 = 0$. On the other hand, because the term $\theta t (\lambda_\phi \sigma_0 \otimes \tau_1 + 2 \sigma_0 \otimes \tau_2)$ anticommutes with both $m \sigma_3 \otimes \tau_3$ and $p_x \sigma_0 \otimes \tau_3$, we expect that a sufficiently large θ opens a gap for a given m .

APPENDIX C: DETAILS OF FINITE-SIZE SCALING ANALYSIS

Figures 26 and 27 show δ^2 dependence of the normalized localization lengths Λ_\perp and Λ_\parallel for the one-dimensional cuts “B” and “C,” respectively. Tables II–VIII present the values of the sets of parameters used in finite-size scaling analysis.

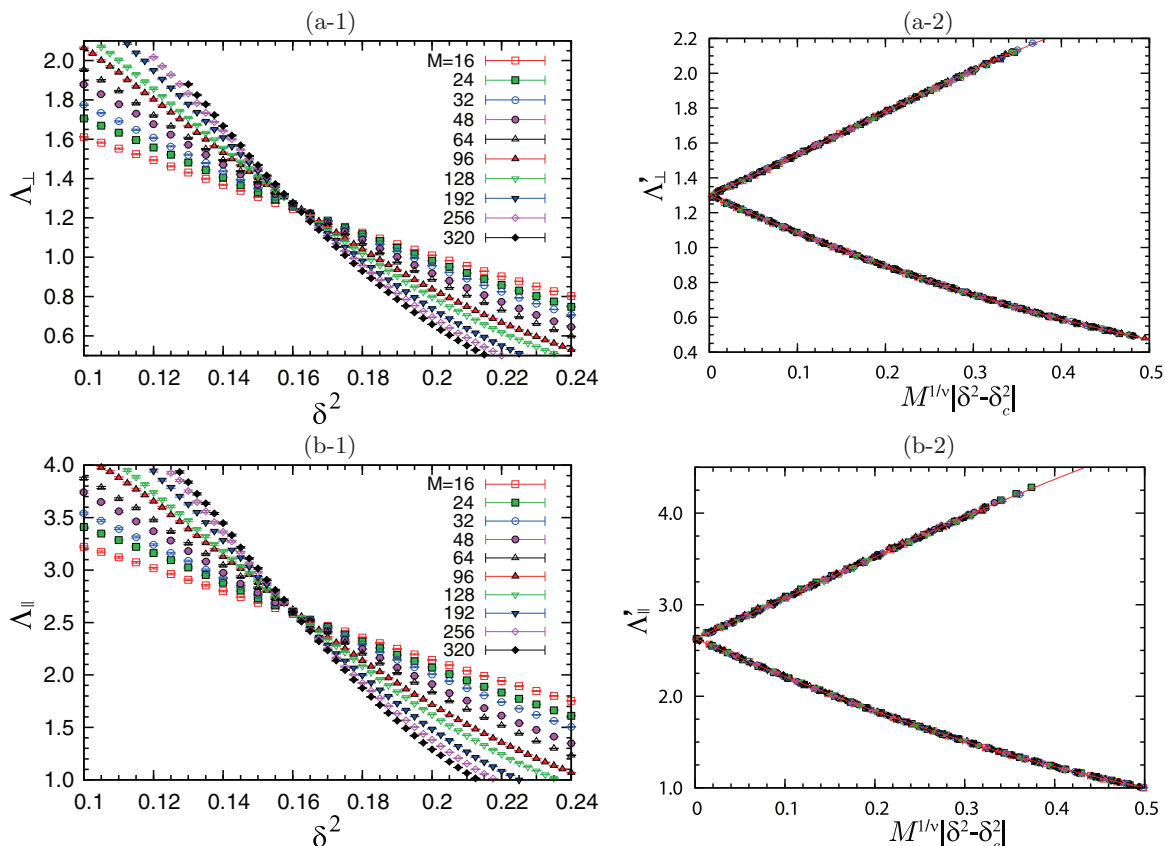


FIG. 26. (Color online) The two-dimensional spin-directed \mathbb{Z}_2 network model is solved numerically along the one-dimensional cut (3.20) in the three-dimensional parameter space (2.7). Panel (a-1) shows the δ^2 dependence of the normalized localization length Λ_\perp corresponding to the geometry of Fig. 13(a) for several values of M . Panel (b-1) shows the δ^2 dependence of the normalized localization lengths Λ_\parallel corresponding to the geometry of Fig. 13(b) for several values of M . A finite-size scaling analysis of panels (a-1) and (b-1) is performed in panels (a-2) and (b-2), respectively. The horizontal axis is $M^{1/\nu} |\delta^2 - \delta_c^2|$ with ν and δ_c^2 given in Tables IV and V. The vertical axis Λ'_x with $x = \perp, \parallel$ is defined by subtracting from the normalized localization length Λ_x its finite-size correction from the leading irrelevant exponent y given in Tables IV and V. The red solid curve demonstrates the quality of the data collapse onto a one-parameter scaling function.

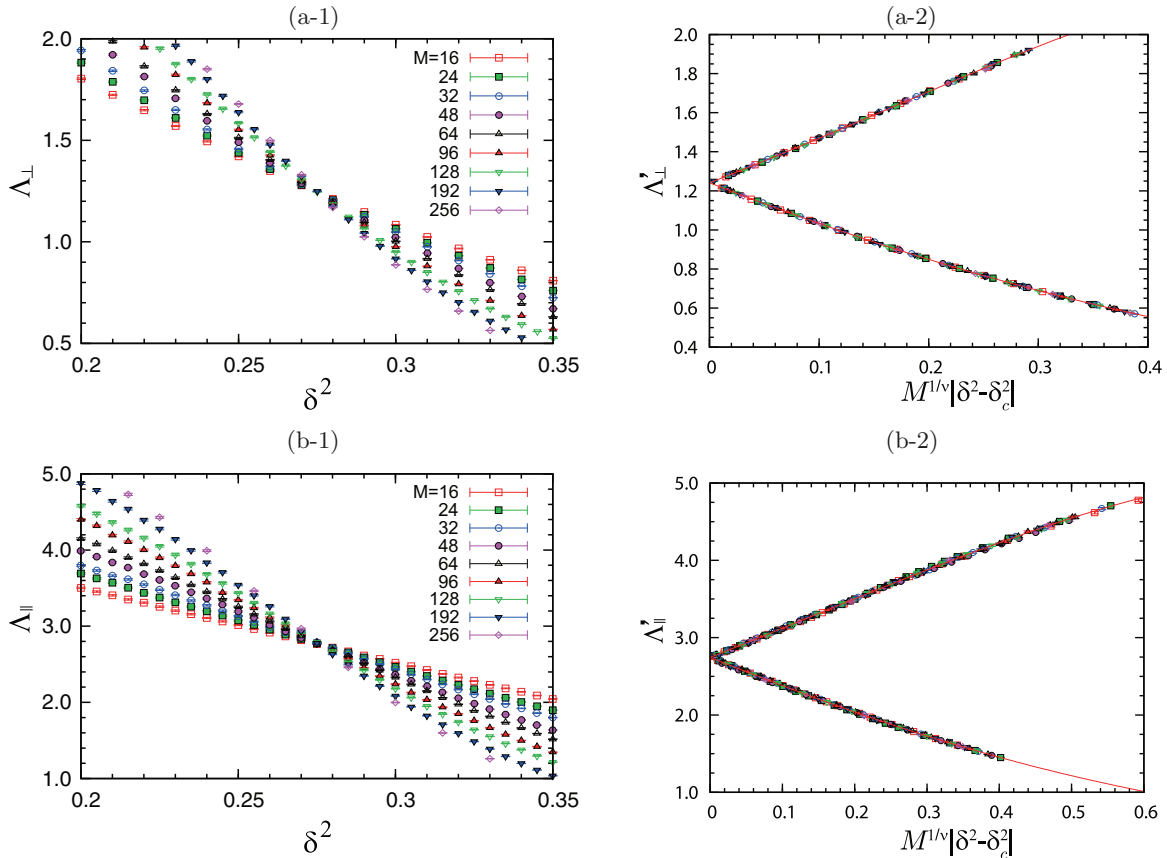


FIG. 27. (Color online) The two-dimensional spin-directed \mathbb{Z}_2 network model is solved numerically along the one-dimensional cut (3.21) in the three-dimensional parameter space (2.7). Panel (a-1) shows the δ^2 dependence of the normalized localization length Λ_{\perp} corresponding to the geometry of Fig. 13(a) for several values of M . Panel (b-1) shows the δ^2 dependence of the normalized localization lengths Λ_{\parallel} corresponding to the geometry of Fig. 13(b) for several values of M . A finite-size scaling analysis of panels (a-1) and (b-1) is performed in panels (a-2) and (b-2), respectively. The horizontal axis is $M^{1/\nu}|\delta^2 - \delta_c^2|$ with ν and δ_c^2 given in Tables VI and VII. The vertical axis Λ'_x with $x = \perp, \parallel$ is defined by subtracting from the normalized localization length Λ_x its finite-size correction from the leading irrelevant exponent y given in Tables VI and VII. The red solid curve demonstrates the quality of the data collapse onto a one-parameter scaling function.

TABLE II. Finite-size scaling analysis of Λ_{\perp} for the two-dimensional spin-directed \mathbb{Z}_2 network model along the cut (3.17) [A: $(0.5, \pi/4, \delta^2)$ for $\delta^2 \in [0, 0.5]$]. Only the values of Λ_{\perp} satisfying $0.35 < \Lambda_{\perp} < 1.7$ enter the data set. Different data sets are chosen by varying the minimum M_{\min} and maximum M_{\max} taken by the width M of the two-dimensional spin-directed \mathbb{Z}_2 network model. The quality of fit is measured by χ_{\min}^2/N and \mathcal{G} . The values ν , y , δ_c^2 , Λ_{\perp}^c , $F_{\perp}^{p,0}$, and $f_{\perp}^{p,q}$ for the fitting parameters and their χ_{\min}^2/N are shown. The numbers with \pm are the statistical error bars (one sigma).

M_{\min}	M_{\max}	N	χ_{\min}^2/N	\mathcal{G}	ν	$ y $	δ_c^2	$\Lambda_{\perp}^c \equiv (1/F_{\perp}^{0,0})$	$f_{\perp}^{0,1}$	$f_{\perp}^{0,2}$	$F_{\perp}^{1,0}$	$f_{\perp}^{1,1}$	$f_{\perp}^{1,2}$	$F_{\perp}^{2,0}$	$f_{\perp}^{2,1}$	$f_{\perp}^{2,2}$	$F_{\perp}^{3,0}$	$f_{\perp}^{3,1}$	$F_{\perp}^{4,0}$	$f_{\perp}^{4,1}$
16	320	461	1.009	0.246	2.922	0.712	0.2336	0.94135	0.2081	-1.132	2.060	1.567	-6.563	3.079	1.644	-2.246	2.803	5.169	0.993	31.085
					± 0.037	± 0.054	± 0.0002	± 0.00256	± 0.0323	± 0.302	± 0.065	± 0.108	± 1.397	± 0.175	± 0.210	± 0.918	± 0.272	± 0.279	± 0.257	± 4.513
24	320	402	0.920	0.714	2.926	0.788	0.2340	0.93539	0.1443	-0.937	2.090	1.883	-11.030	3.131	2.053	-5.646	2.903	6.115	1.102	36.256
					± 0.053	± 0.107	± 0.0002	± 0.00299	± 0.0766	± 0.803	± 0.090	± 0.283	± 6.088	± 0.251	± 0.406	± 4.032	± 0.392	± 0.876	± 0.364	± 5.269
32	320	361	0.946	0.543	2.850	0.728	0.2345	0.92583	-0.0657	0.683	1.989	2.028	-9.519	2.802	2.768	-6.529	2.434	6.600	0.845	33.365
					± 0.102	± 0.159	± 0.0004	± 0.00636	± 0.0955	± 0.670	± 0.174	± 0.425	± 8.209	± 0.481	± 0.630	± 6.497	± 0.698	± 1.015	± 0.544	± 6.811
16	256	421	1.043	0.118	2.880	0.675	0.2337	0.94084	0.1907	-0.948	1.994	1.647	-5.943	2.892	1.805	-2.000	2.510	5.481	0.789	34.324
					± 0.052	± 0.057	± 0.0002	± 0.00344	± 0.0353	± 0.260	± 0.092	± 0.144	± 1.183	± 0.239	± 0.271	± 0.848	± 0.359	± 0.395	± 0.320	± 8.998
24	256	362	0.947	0.539	2.845	0.701	0.2343	0.93049	0.0569	-0.314	1.970	1.903	-7.757	2.777	2.356	-4.043	2.361	6.403	0.725	39.007
					± 0.089	± 0.108	± 0.0003	± 0.00487	± 0.0728	± 0.441	± 0.153	± 0.242	± 3.745	± 0.407	± 0.490	± 2.723	± 0.591	± 0.621	± 0.477	± 12.878

TABLE III. Finite-size scaling analysis of Λ_{\perp} for the two-dimensional spin-directed \mathbb{Z}_2 network model along the cut (3.17) [A: $(0.5, \pi/4, \delta^2)$ for $\delta^2 \in [0, 0.5]$]. Only the values of Λ_{\parallel} satisfying $1.4 < \Lambda_{\perp} < 6.0$ enter the data set. Different data sets are chosen by varying the minimum M_{\min} and maximum M_{\max} taken by the width M of the two-dimensional spin-directed \mathbb{Z}_2 network model. The quality of fit is measured by χ_{\min}^2/N and \mathcal{G} . The values ν , y , δ_c^2 , Λ_{\parallel}^c , $F_{\parallel}^{p,0}$, and $f_{\parallel}^{p,q}$ for the fitting parameters and their χ_{\min}^2/N are shown. The numbers with \pm are the statistical error bars (one sigma).

M_{\min}	M_{\max}	N	χ_{\min}^2/N	\mathcal{G}	ν	$ y $	δ_c^2	$\Lambda_{\parallel}^c \equiv (1/F_{\parallel}^{0,0})$	$f_{\parallel}^{0,1}$	$F_{\parallel}^{1,0}$	$f_{\parallel}^{1,1}$	$F_{\parallel}^{2,0}$	$f_{\parallel}^{2,1}$	$F_{\parallel}^{3,0}$	$f_{\parallel}^{3,1}$	$F_{\parallel}^{4,0}$	$f_{\parallel}^{4,1}$
16	256	403	0.941	0.641	2.793	0.404	0.2336	3.70707	0.041	0.562	-0.789	0.954	-0.967	1.004	-0.974	0.626	-0.735
					± 0.052	± 0.053	± 0.0003	± 0.01882	± 0.010	± 0.031	± 0.034	± 0.096	± 0.041	± 0.147	± 0.094	± 0.135	± 0.442
24	256	352	0.970	0.450	2.758	0.387	0.2340	3.67677	0.013	0.556	-0.745	0.903	-0.807	0.920	-0.774	0.615	-0.972
					± 0.067	± 0.083	± 0.0003	± 0.02158	± 0.014	± 0.045	± 0.055	± 0.129	± 0.065	± 0.186	± 0.149	± 0.168	± 0.397
32	256	307	0.875	0.852	2.653	0.473	0.2352	3.58849	-0.088	0.511	-0.801	0.747	-0.580	0.709	-0.547	0.444	-1.156
					± 0.059	± 0.125	± 0.0003	± 0.02051	± 0.030	± 0.039	± 0.146	± 0.093	± 0.130	± 0.127	± 0.257	± 0.117	± 0.740
16	192	361	0.943	0.606	2.772	0.449	0.2335	3.71150	0.049	0.543	-0.828	0.904	-1.008	0.924	-0.948	0.576	-0.659
					± 0.063	± 0.068	± 0.0003	± 0.02286	± 0.012	± 0.034	± 0.052	± 0.104	± 0.055	± 0.153	± 0.128	± 0.140	± 0.586
24	192	310	0.980	0.381	2.702	0.476	0.2340	3.67609	0.016	0.517	-0.818	0.799	-0.803	0.767	-0.595	0.514	-0.980
					± 0.073	± 0.114	± 0.0004	± 0.02398	± 0.019	± 0.041	± 0.115	± 0.113	± 0.094	± 0.152	± 0.249	± 0.143	± 0.595
32	192	265	0.866	0.842	2.578	0.632	0.2356	3.57956	-0.157	0.472	-1.038	0.646	-0.394	0.573	-0.045	0.362	-1.722
					± 0.051	± 0.175	± 0.0003	± 0.02268	± 0.073	± 0.029	± 0.361	± 0.063	± 0.250	± 0.080	± 0.566	± 0.082	± 1.415

TABLE IV. Finite-size scaling analysis of Λ_{\perp} for the two-dimensional spin-directed \mathbb{Z}_2 network model along the cut (3.20) [B: $(0.5, 5\pi/16, \delta^2)$ for $\delta^2 \in [0, 0.5]$]. Only the values of Λ_{\perp} satisfying $0.45 < \Lambda_{\perp} < 2.15$ enter the data set. Different data sets are chosen by varying the minimum M_{\min} and maximum M_{\max} taken by the width M of the two-dimensional spin-directed \mathbb{Z}_2 network model. The quality of fit is measured by χ_{\min}^2/N and \mathcal{G} . The values ν , y , δ_c^2 , Λ_{\perp}^c , $F_{\perp}^{p,0}$, and $f_{\perp}^{p,q}$ for the fitting parameters and their χ_{\min}^2/N are shown. The numbers with \pm are the statistical error bars (one sigma).

M_{\min}	M_{\max}	N	χ_{\min}^2/N	\mathcal{G}	ν	$ y $	δ_c^2	$\Lambda_{\perp}^c \equiv (1/F_{\perp}^{0,0})$	$f_{\perp}^{0,1}$	$f_{\perp}^{0,2}$	$F_{\perp}^{1,0}$	$f_{\perp}^{1,1}$	$f_{\perp}^{1,2}$	$F_{\perp}^{2,0}$	$f_{\perp}^{2,1}$	$F_{\perp}^{3,0}$	$f_{\perp}^{3,1}$	$F_{\perp}^{4,0}$
12	320	528	1.067	0.064	2.743	0.580	0.1588	1.30050	0.0919	0.446	1.332	1.204	-4.489	1.741	1.515	1.439	0.887	0.999
					± 0.021	± 0.032	± 0.0002	± 0.00381	± 0.0354	± 0.051	± 0.030	± 0.083	± 0.344	± 0.072	± 0.072	± 0.086	± 0.190	± 0.046
16	320	477	1.019	0.223	2.731	0.625	0.1595	1.28399	-0.0079	0.911	1.350	1.162	-5.039	1.743	1.722	1.428	1.015	0.960
					± 0.025	± 0.045	± 0.0002	± 0.00500	± 0.0497	± 0.109	± 0.033	± 0.080	± 0.735	± 0.085	± 0.079	± 0.098	± 0.215	± 0.054
32	320	373	0.751	0.999	2.688	0.729	0.1611	1.24759	-0.4620	4.587	1.362	1.361	-8.908	1.722	2.422	1.364	1.643	0.717
					± 0.045	± 0.111	± 0.0005	± 0.01359	± 0.0893	± 2.293	± 0.050	± 0.208	± 5.160	± 0.144	± 0.323	± 0.163	± 0.389	± 0.086
12	256	491	1.040	0.139	2.765	0.613	0.1584	1.30826	0.1600	0.343	1.357	1.143	-4.870	1.806	1.486	1.498	0.885	1.066
					± 0.025	± 0.041	± 0.0002	± 0.00417	± 0.0457	± 0.069	± 0.036	± 0.105	± 0.483	± 0.087	± 0.081	± 0.101	± 0.211	± 0.055
16	256	440	0.974	0.453	2.867	1.413	0.1592	1.28935	2.1767	-35.927	1.529	0.119	-86.394	2.219	6.329	1.906	0.946	1.322
					± 0.006	± 0.080	± 0.0001	± 0.00206	± 0.5515	± 21.322	± 0.006	± 0.384	± 27.812	± 0.018	± 1.310	± 0.023	± 0.906	± 0.032
12	192	450	0.863	0.952	2.905	1.118	0.1581	1.30627	1.1074	-5.450	1.540	0.063	-18.218	2.271	2.295	1.987	0.220	1.435
					± 0.008	± 0.069	± 0.0002	± 0.00391	± 0.1953	± 2.435	± 0.009	± 0.227	± 3.708	± 0.025	± 0.338	± 0.031	± 0.361	± 0.034
16	192	399	0.822	0.984	2.883	1.307	0.1587	1.29607	1.7245	-19.092	1.535	-0.022	-48.366	2.237	4.543	1.924	1.295	1.377
					± 0.009	± 0.095	± 0.0002	± 0.00330	± 0.4923	± 13.253	± 0.009	± 0.422	± 16.502	± 0.026	± 1.051	± 0.032	± 0.768	± 0.036

TABLE V. Finite-size scaling analysis of Λ_{\perp} for the two-dimensional spin-directed \mathbb{Z}_2 network model along the cut (3.20) [B: $(0.5, 5\pi/16, \delta^2)$ for $\delta^2 \in [0, 0.5]$]. Only the values of Λ_{\parallel} satisfying $1.0 < \Lambda_{\parallel} < 4.0$ enter the data set. Different data sets are chosen by varying the minimum M_{\min} and maximum M_{\max} taken by the width M of the two-dimensional spin-directed \mathbb{Z}_2 network model. The quality of fit is measured by χ_{\min}^2/N and \mathcal{G} . The values ν , y , δ_c^2 , Λ_{\parallel}^c , $F_{\parallel}^{p,0}$, and $f_{\parallel}^{p,q}$ for the fitting parameters and their χ_{\min}^2/N are shown. The numbers with \pm are the statistical error bars (one sigma).

M_{\min}	M_{\max}	N	χ_{\min}^2/N	\mathcal{G}	ν	$ y $	δ_c^2	$\Lambda_{\parallel}^c \equiv (1/F_{\parallel}^{0,0})$	$f_{\parallel}^{0,1}$	$F_{\parallel}^{1,0}$	$f_{\parallel}^{1,1}$	$F_{\parallel}^{2,0}$	$f_{\parallel}^{2,1}$	$F_{\parallel}^{3,0}$	$f_{\parallel}^{3,1}$	$F_{\parallel}^{4,0}$	$f_{\parallel}^{4,1}$
16	320	450	0.926	0.752	2.585	1.355	0.1595	2.63191	0.812	0.622	-3.609	0.835	-2.811	0.667	-17.095	0.266	28.211
					± 0.008	± 0.057	± 0.0001	± 0.00344	± 0.105	± 0.003	± 0.498	± 0.010	± 0.504	± 0.017	± 2.850	± 0.028	± 13.114
24	320	392	0.925	0.717	2.627	1.102	0.1591	2.64418	0.476	0.640	-1.779	0.888	-2.039	0.751	-10.540	0.312	4.511
					± 0.018	± 0.115	± 0.0002	± 0.00677	± 0.129	± 0.008	± 0.516	± 0.024	± 0.514	± 0.041	± 3.242	± 0.039	± 7.585
32	320	341	0.987	0.358	2.637	1.089	0.1590	2.64916	0.544	0.643	-1.715	0.902	-2.504	0.768	-10.699	0.326	4.774
					± 0.028	± 0.202	± 0.0002	± 0.01055	± 0.282	± 0.012	± 0.916	± 0.039	± 1.139	± 0.064	± 6.135	± 0.048	± 11.316
48	320	295	1.096	0.045	2.625	1.387	0.1591	2.64608	1.670	0.638	-5.847	0.882	-5.912	0.711	-12.797	0.359	-50.833
					± 0.035	± 0.478	± 0.0003	± 0.01358	± 2.519	± 0.016	± 9.286	± 0.048	± 7.724	± 0.065	± 19.002	± 0.065	± 102.505
16	256	415	0.904	0.827	2.588	1.333	0.1593	2.63549	0.801	0.623	-3.449	0.837	-2.656	0.666	-15.829	0.267	25.730
					± 0.010	± 0.062	± 0.0001	± 0.00428	± 0.109	± 0.004	± 0.509	± 0.012	± 0.489	± 0.020	± 2.812	± 0.030	± 12.860
24	256	357	0.911	0.760	2.663	0.947	0.1587	2.66138	0.376	0.654	-1.280	0.934	-1.647	0.822	-6.982	0.342	2.410
					± 0.029	± 0.127	± 0.0003	± 0.01149	± 0.101	± 0.013	± 0.365	± 0.041	± 0.375	± 0.071	± 2.208	± 0.052	± 5.035
32	256	306	0.970	0.427	2.721	0.763	0.1581	2.68761	0.307	0.679	-0.869	1.021	-1.455	0.952	-4.433	0.421	0.027
					± 0.068	± 0.217	± 0.0005	± 0.02842	± 0.131	± 0.033	± 0.373	± 0.112	± 0.502	± 0.190	± 2.298	± 0.106	± 3.875
16	192	377	0.886	0.867	2.561	1.464	0.1596	2.62681	1.038	0.613	-4.543	0.812	-3.431	0.628	-22.355	0.233	51.727
					± 0.011	± 0.074	± 0.0002	± 0.00483	± 0.169	± 0.004	± 0.803	± 0.013	± 0.748	± 0.020	± 4.719	± 0.029	± 23.579
24	192	319	0.920	0.686	2.638	1.062	0.1589	2.65335	0.491	0.642	-1.591	0.907	-2.226	0.777	-9.744	0.280	10.521
					± 0.033	± 0.161	± 0.0004	± 0.01315	± 0.172	± 0.014	± 0.593	± 0.044	± 0.687	± 0.074	± 4.032	± 0.050	± 10.589
32	192	268	0.982	0.349	2.697	0.889	0.1582	2.68162	0.442	0.664	-1.065	0.991	-2.178	0.903	-6.721	0.313	8.302
					± 0.081	± 0.301	± 0.0007	± 0.03407	± 0.287	± 0.035	± 0.681	± 0.123	± 1.278	± 0.206	± 5.229	± 0.088	± 12.495

TABLE VI. Finite-size scaling analysis of Λ_{\perp} for the two-dimensional spin-directed \mathbb{Z}_2 network model along the cut (3.21) [C: $(0.6, \pi/4, \delta^2)$ for $\delta^2 \in [0, 0.4]$]. Only the values of Λ_{\perp} satisfying $0.5 < \Lambda_{\perp} < 2.0$ enter the data set. Different data sets are chosen by varying the minimum M_{\min} and maximum M_{\max} taken by the width M of the two-dimensional spin-directed \mathbb{Z}_2 network model. The quality of fit is measured by χ_{\min}^2/N and \mathcal{G} . The values ν , y , δ_c^2 , Λ_{\perp}^c , $F_{\perp}^{p,0}$, and $f_{\perp}^{p,q}$ for the fitting parameters and their χ_{\min}^2/N are shown. The numbers with \pm are the statistical error bars (one sigma).

M_{\min}	M_{\max}	N	χ_{\min}^2/N	\mathcal{G}	ν	$ y $	δ_c^2	$\Lambda_{\perp}^c \equiv (1/F_{\perp}^{0,0})$	$f_{\perp}^{0,1}$	$f_{\perp}^{0,2}$	$F_{\perp}^{1,0}$	$f_{\perp}^{1,1}$	$f_{\perp}^{1,2}$	$F_{\perp}^{2,0}$	$f_{\perp}^{2,1}$	$F_{\perp}^{3,0}$	$f_{\perp}^{3,1}$	$F_{\perp}^{4,0}$
16	256	172	0.570	1.000	2.837	0.713	0.2756	1.24122	0.1135	-0.861	1.420	1.861	-5.834	1.852	1.835	1.507	3.884	1.226
					± 0.069	± 0.138	± 0.0004	± 0.00760	± 0.0579	± 0.523	± 0.097	± 0.280	± 3.660	± 0.223	± 0.205	± 0.302	± 0.639	± 0.205
24	256	150	0.536	1.000	2.810	0.764	0.2763	1.22920	-0.0080	-0.374	1.416	2.138	-8.279	1.814	2.293	1.436	5.463	1.098
					± 0.107	± 0.253	± 0.0005	± 0.00993	± 0.1141	± 0.916	± 0.139	± 0.949	± 12.369	± 0.337	± 0.555	± 0.453	± 1.618	± 0.280
16	192	162	0.513	1.000	2.865	0.819	0.2764	1.22782	0.0032	-0.729	1.487	1.993	-8.833	1.973	2.006	1.674	4.180	1.323
					± 0.068	± 0.163	± 0.0004	± 0.00701	± 0.0752	± 0.638	± 0.084	± 0.453	± 6.916	± 0.206	± 0.308	± 0.285	± 0.899	± 0.215
24	192	140	0.426	1.000	2.830	0.938	0.2776	1.20775	-0.4189	3.267	1.493	2.702	-19.406	1.938	3.108	1.599	7.578	1.167
					± 0.094	± 0.270	± 0.0008	± 0.01461	± 0.2471	± 4.782	± 0.098	± 1.621	± 32.971	± 0.264	± 1.190	± 0.365	± 3.573	± 0.260

TABLE VII. Finite-size scaling analysis of Λ_{\parallel} for the two-dimensional spin-directed \mathbb{Z}_2 network model along the cut (3.21) [C: $(0.6, \pi/4, \delta^2)$ for $\delta^2 \in [0, 0.4]$]. Only the values of Λ_{\perp} satisfying $1.5 < \Lambda_{\parallel} < 4.5$ enter the data set. Different data sets are chosen by varying the minimum M_{\min} and maximum M_{\max} taken by the width M of the two-dimensional spin-directed \mathbb{Z}_2 network model. The quality of fit is measured by χ_{\min}^2/N and \mathcal{G} . The values ν , y , δ_c^2 , Λ_{\parallel}^c , $F_{\parallel}^{p,0}$, and $f_{\parallel}^{p,q}$ for the fitting parameters and their χ_{\min}^2/N are shown. The numbers with \pm are the statistical error bars (one sigma).

M_{\min}	M_{\max}	N	χ_{\min}^2/N	\mathcal{G}	ν	$ y $	δ_c^2	$\Lambda_{\parallel}^c \equiv (1/F_{\parallel}^{0,0})$	$f_{\parallel}^{0,1}$	$f_{\parallel}^{0,2}$	$F_{\parallel}^{1,0}$	$f_{\parallel}^{1,1}$	$f_{\parallel}^{1,2}$	$F_{\parallel}^{2,0}$	$f_{\parallel}^{2,1}$	$F_{\parallel}^{3,0}$	$f_{\parallel}^{3,1}$	$F_{\parallel}^{4,0}$
16	256	284	0.993	0.295	2.513	0.877	0.2765	2.74397	-0.1021	0.750	0.495	-1.312	-0.003	0.581	-1.405	0.433	-1.473	0.190
					± 0.068	± 0.560	± 0.0004	± 0.01498	± 0.1312	± 2.186	± 0.039	± 1.985	± 4.992	± 0.084	± 1.386	± 0.081	± 1.542	± 0.032
24	256	238	0.864	0.804	2.642	0.768	0.2760	2.75834	-0.0674	0.770	0.556	-2.241	8.971	0.717	-1.997	0.593	-2.545	0.256
					± 0.080	± 0.225	± 0.0006	± 0.02421	± 0.1548	± 1.371	± 0.046	± 1.089	± 12.120	± 0.105	± 0.772	± 0.121	± 1.123	± 0.051
16	192	277	0.981	0.341	2.483	0.991	0.2767	2.73993	-0.1617	1.569	0.481	-1.585	-0.150	0.553	-1.588	0.405	-1.700	0.177
					± 0.066	± 0.732	± 0.0005	± 0.01841	± 0.2463	± 5.887	± 0.038	± 3.232	± 9.851	± 0.077	± 2.188	± 0.073	± 2.482	± 0.030
24	192	231	0.859	0.813	2.644	0.747	0.2764	2.74260	-0.1485	1.149	0.563	-2.229	8.454	0.727	-1.944	0.605	-2.513	0.256
					± 0.097	± 0.260	± 0.0008	± 0.03223	± 0.1824	± 1.784	± 0.060	± 1.169	± 12.712	± 0.132	± 0.845	± 0.151	± 1.257	± 0.059

TABLE VIII. Finite-size scaling analysis of Λ_{\parallel} for the two-dimensional spin-directed \mathbb{Z}_2 network model along the cut (3.23) [D: (0.5, θ , 0.234)]. Only the values of Λ_{\parallel} satisfying $2.0 < \Lambda_{\parallel} < 5.0$ enter the data set. Different data sets are chosen by varying the minimum M_{\min} and maximum M_{\max} taken by the width M of the two-dimensional spin-directed \mathbb{Z}_2 network model. The quality of fit is measured by χ_{\min}^2/N and \mathcal{G} . According to the scaling analysis along the one-dimensional cut (3.17), we use the values $\theta_c/\pi = 0.25$ and $\Lambda_{\parallel}^c = 0.3657$ shown in Table I as the known numbers. The values ν , y , $F_{\parallel}^{p,0}$, and $f_{\parallel}^{p,q}$ for the fitting parameters and their χ_{\min}^2/N are shown. The numbers with \pm are the statistical error bars (one sigma).

M_{\min}	M_{\max}	N	χ_{\min}^2/N	\mathcal{G}	ν	$ y $	$\theta_c/\pi^{(*)}$	$\Lambda_{\parallel}^c \equiv 1/F_{\parallel}^{0,0^{(*)}}$	$f_{\parallel}^{1,1}$	$f_{\parallel}^{1,2}$	$F_{\parallel}^{2,0}$	$f_{\parallel}^{2,1}$	$F_{\parallel}^{3,0}$	$F_{\parallel}^{4,0}$
16	256	78	0.794	0.742	2.872	0.387	0.2500	3.65700	-0.0374	0.095	0.356	1.025	0.375	0.141
					± 0.045	± 0.046			± 0.0062	± 0.019	± 0.024	± 0.116	± 0.017	± 0.029
24	256	66	0.905	0.414	2.866	0.329	0.2500	3.65700	-0.0328	0.072	0.339	1.034	0.373	0.141
					± 0.054	± 0.066			± 0.0076	± 0.025	± 0.035	± 0.169	± 0.019	± 0.031
32	256	55	0.943	0.290	2.912	0.299	0.2500	3.65700	-0.0188	0.026	0.346	0.932	0.390	0.151
					± 0.067	± 0.110			± 0.0104	± 0.027	± 0.055	± 0.223	± 0.025	± 0.035
48	256	45	0.826	0.461	2.882	0.678	0.2500	3.65700	-0.1157	0.869	0.391	1.700	0.379	0.142
					± 0.080	± 0.176			± 0.0679	± 0.971	± 0.032	± 0.517	± 0.030	± 0.036
16	192	73	0.778	0.755	2.862	0.417	0.2500	3.65700	-0.0394	0.107	0.362	1.035	0.373	0.137
					± 0.047	± 0.052			± 0.0069	± 0.024	± 0.024	± 0.114	± 0.017	± 0.030
24	192	61	0.909	0.382	2.855	0.372	0.2500	3.65700	-0.0365	0.090	0.350	1.032	0.370	0.137
					± 0.057	± 0.080			± 0.0091	± 0.035	± 0.035	± 0.152	± 0.020	± 0.031
32	192	50	0.967	0.232	2.908	0.367	0.2500	3.65700	-0.0220	0.035	0.365	0.914	0.388	0.152
					± 0.072	± 0.140			± 0.0136	± 0.042	± 0.050	± 0.170	± 0.026	± 0.036

- [1] F. D. M. Haldane, *Phys. Rev. Lett.* **61**, 2015 (1988).
- [2] D. J. Thouless, M. Kohmoto, M. P. Nightingale, and M. den Nijs, *Phys. Rev. Lett.* **49**, 405 (1982).
- [3] B. I. Halperin, *Phys. Rev. B* **25**, 2185 (1982).
- [4] C. L. Kane and E. J. Mele, *Phys. Rev. Lett.* **95**, 226801 (2005).
- [5] C. L. Kane and E. J. Mele, *Phys. Rev. Lett.* **95**, 146802 (2005).
- [6] H. Suzuura and T. Ando, *Phys. Rev. Lett.* **89**, 266603 (2002).
- [7] T. Ando and H. Suzuura, *J. Phys. Soc. Jpn.* **71**, 2753 (2002).
- [8] Y. Takane, *J. Phys. Soc. Jpn.* **73**, 9 (2004); **73**, 1430 (2004); **73**, 2366 (2004).
- [9] B. I. Halperin, *Jpn. J. Appl. Phys. Suppl.* **26**(26-3), 1913 (1987).
- [10] J. T. Chalker and A. Dohmen, *Phys. Rev. Lett.* **75**, 4496 (1995).
- [11] L. Balents and M. P. A. Fisher, *Phys. Rev. Lett.* **76**, 2782 (1996).
- [12] Y. B. Kim, *Phys. Rev. B* **53**, 16420 (1996).
- [13] H. Mathur, *Phys. Rev. Lett.* **78**, 2429 (1997).
- [14] I. A. Gruzberg, N. Read, and S. Sachdev, *Phys. Rev. B* **55**, 10593 (1997); **56**, 13218 (1997).
- [15] S. Cho, L. Balents, and M. P. A. Fisher, *Phys. Rev. B* **56**, 15814 (1997).
- [16] L. Balents, M. P. A. Fisher, and M. R. Zirnbauer, *Nucl. Phys B* **483**, 601 (1997).
- [17] D. P. Druiet, P. J. Turley, K. D. Maranowski, E. G. Gwinn, and A. C. Gossard, *Phys. Rev. Lett.* **80**, 365 (1998).
- [18] L. Fu, C. L. Kane, and E. J. Mele, *Phys. Rev. Lett.* **98**, 106803 (2007).
- [19] J. E. Moore and L. Balents, *Phys. Rev. B* **75**, 121306(R) (2007).
- [20] R. Roy, *Phys. Rev. B* **79**, 195321 (2009); **79**, 195322 (2009).
- [21] L. Fu and C. L. Kane, *Phys. Rev. B* **76**, 045302 (2007).
- [22] D. Hsieh, D. Qian, L. Wray, Y. Xia, Y. S. Hor, R. J. Cava, and M. Z. Hasan, *Nature (London)* **452**, 970 (2008).
- [23] Y. Xia, L. Wray, D. Qian, D. Hsieh, A. Pal, H. Lin, A. Bansil, D. Grauer, Y. Hor, R. Cava, and M. Z. Hasan, *Nat. Phys.* **5**, 398 (2009).
- [24] Y. L. Chen, J. G. Analytis, J. H. Chu, Z. K. Liu, S.-K. Mo, X. L. Qi, H. J. Zhang, D. H. Lu, X. Dai, Z. Fang, S. C. Zhang, I. R. Fisher, Z. Hussain, and Z.-X. Shen, *Science* **325**, 178 (2009).
- [25] H. Lin, R. S. Markiewicz, L. A. Wray, L. Fu, M. Z. Hasan, and A. Bansil, *Phys. Rev. Lett.* **105**, 036404 (2010).
- [26] T. Sato, K. Segawa, H. Guo, K. Sugawara, S. Souma, T. Takahashi, and Y. Ando, *Phys. Rev. Lett.* **105**, 136802 (2010).
- [27] K. Kuroda, M. Ye, A. Kimura, S. V. Ereemeev, E. E. Krasovskii, E. V. Chulkov, Y. Ueda, K. Miyamoto, T. Okuda, K. Shimada, H. Namatame, and M. Taniguchi, *Phys. Rev. Lett.* **105**, 146801 (2010).
- [28] Y. L. Chen, Z. K. Liu, J. G. Analytis, J.-H. Chu, H. J. Zhang, B. H. Yan, S.-K. Mo, R. G. Moore, D. H. Lu, I. R. Fisher, S. C. Zhang, Z. Hussain, and Z.-X. Shen, *Phys. Rev. Lett.* **105**, 266401 (2010).
- [29] B. Rasche, A. Isaeva, M. Ruck, S. Borisenko, V. Zabolotnyy, B. Büchner, K. Koepf, C. Ortix, M. Richter, and J. van den Brink, *Nat. Mater.* **12**, 422 (2013).
- [30] P. M. Ostrovsky, I. V. Gornyi, and A. D. Mirlin, *Phys. Rev. Lett.* **98**, 256801 (2007).
- [31] S. Ryu, C. Mudry, H. Obuse, and A. Furusaki, *Phys. Rev. Lett.* **99**, 116601 (2007).
- [32] The order of limits matters here. We assume that we can describe the disordered surface states of a strong \mathbb{Z}_2 topological insulator by a Dirac Hamiltonian in a two-dimensional representation of the Clifford algebra with all random potentials compatible

with the time-reversal-symmetry white noise correlated. The disorder strength is measured by the variances g^2 of the random potentials. The strong disorder limit by which the variances g^2 are made arbitrarily large within the Dirac approximation presumes that $g \ll \Delta$ still holds whereby Δ is the bulk band gap. The opposite limit for which the disorder strength is larger than the bulk band gap destroys all topological attributes.

- [33] J. H. Bardarson, J. Tworzydło, P. W. Brouwer, and C. W. J. Beenakker, *Phys. Rev. Lett.* **99**, 106801 (2007).
- [34] K. Nomura, M. Koshino, and S. Ryu, *Phys. Rev. Lett.* **99**, 146806 (2007).
- [35] C.-X. Liu, X.-L. Qi, and S.-C. Zhang, *Phys. E (Amsterdam)* **44**, 906 (2012).
- [36] R. S. K. Mong, J. H. Bardarson, and J. E. Moore, *Phys. Rev. Lett.* **108**, 076804 (2012).
- [37] L. Fu and C. L. Kane, *Phys. Rev. Lett.* **109**, 246605 (2012).
- [38] T. Morimoto and A. Furusaki, *Phys. Rev. B* **88**, 125129 (2013).
- [39] C. Callan and J. A. Harvey, *Nucl. Phys. B* **250**, 427 (1985).
- [40] Z. Ringel, Y. E. Kraus, and A. Stern, *Phys. Rev. B* **86**, 045102 (2012).
- [41] K. Kobayashi, T. Ohtsuki, and K.-I. Imura, *Phys. Rev. Lett.* **110**, 236803 (2013).
- [42] H. Obuse, A. Furusaki, S. Ryu, and C. Mudry, *Phys. Rev. B* **76**, 075301 (2007).
- [43] H. Obuse, A. Furusaki, S. Ryu, and C. Mudry, *Phys. Rev. B* **78**, 115301 (2008).
- [44] S. Ryu, C. Mudry, H. Obuse, and A. Furusaki, *New J. Phys.* **12**, 065005 (2010).
- [45] See Supplemental Material at <http://link.aps.org/supplemental/10.1103/PhysRevB.89.155315> for detailed derivations of the two-dimensional Dirac Hamiltonians.
- [46] V. M. Yakovenko, *Phys. Rev. B* **43**, 11353 (1991).
- [47] D.-H. Lee, *Phys. Rev. B* **50**, 10788 (1994).
- [48] C. L. Kane, R. Mukhopadhyay, and T. C. Lubensky, *Phys. Rev. Lett.* **88**, 036401 (2002).
- [49] J. C. Y. Teo and C. L. Kane, *Phys. Rev. B* **89**, 085101 (2014).
- [50] Critical transport in the direction orthogonal to the direction along which transport is perfect (directed) in the directed CC network model for a weak three-dimensional Chern insulator was established by Chalker and Dohmen in Ref. [10]. They quantified how the transport along the direction that corresponds to the stacking direction of a weak three-dimensional Chern insulator depends on the ratio of the height and the perimeter in the cylindrical geometry of Fig. 2.
- [51] J. T. Chalker and P. D. Coddington, *J. Phys. C: Solid State Phys.* **21**, 2665 (1988).
- [52] S. Hikami, A. I. Larkin, and Y. Nagaoka, *Prog. Theor. Phys.* **63**, 707 (1980).
- [53] K. Nomura, S. Ryu, M. Koshino, C. Mudry, and A. Furusaki, *Phys. Rev. Lett.* **100**, 246806 (2008).
- [54] R. J. Johnston and H. Kunz, *J. Phys. C: Solid State Phys.* **16**, 3895 (1983).
- [55] A. MacKinnon and B. Kramer, *Z. Phys. B: Condens. Matter* **53**, 1 (1983).
- [56] See K. Slevin and T. Ohtsuki, *Phys. Rev. Lett.* **82**, 382 (1999) and references therein.
- [57] H. Obuse, S. Bera, A. W. W. Ludwig, I. A. Gruzberg, and F. Evers, *Europhys. Lett.* **104**, 27014 (2013).
- [58] Y. Asada, K. Slevin, and T. Ohtsuki, *Phys. Rev. Lett.* **89**, 256601 (2002).
- [59] J. L. Cardy, in *Phase Transition and Critical Phenomena*, Vol. 11, edited by C. Domb and J. L. Lebowitz (Academic, New York, 1986).
- [60] K.-I. Imura, M. Okamoto, Y. Yoshimura, Y. Takane, and T. Ohtsuki, *Phys. Rev. B* **86**, 245436 (2012).
- [61] Y. Yoshimura, A. Matsumoto, Y. Takane, and K.-I. Imura, *Phys. Rev. B* **88**, 045408 (2013).
- [62] P. W. Brouwer and K. Frahm, *Phys. Rev. B* **53**, 1490 (1996).
- [63] B. Kramer, T. Ohtsuki, and S. Kettemann, *Phys. Rep.* **417**, 211 (2005).
- [64] A. P. Schnyder, S. Ryu, A. Furusaki, and A. W. W. Ludwig, *Phys. Rev. B* **78**, 195125 (2008).
- [65] A. Kitaev, *AIP Conf. Proc.* **1134**, 22 (2009).
- [66] S. Ryu, A. P. Schnyder, A. Furusaki, and A. W. W. Ludwig, *New J. Phys.* **12**, 065010 (2010).
- [67] H. Yao and S. Ryu, *Phys. Rev. B* **88**, 064507 (2013).
- [68] C.-K. Chiu, H. Yao, and S. Ryu, *Phys. Rev. B* **88**, 075142 (2013).
- [69] I. C. Fulga, B. van Heck, J. M. Edge, and A. R. Akhmerov, [arXiv:1212.6191](https://arxiv.org/abs/1212.6191).
- [70] C. Wu, B. A. Bernevig, and S.-C. Zhang, *Phys. Rev. Lett.* **96**, 106401 (2006).
- [71] C. Xu and J. E. Moore, *Phys. Rev. B* **73**, 045322 (2006).
- [72] M. Levin and A. Stern, *Phys. Rev. Lett.* **103**, 196803 (2009).
- [73] L. Fidkowski and A. Kitaev, *Phys. Rev. B* **81**, 134509 (2010).
- [74] L. Fidkowski and A. Kitaev, *Phys. Rev. B* **83**, 075103 (2011).
- [75] A. M. Turner, F. Pollmann, and E. Berg, *Phys. Rev. B* **83**, 075102 (2011).
- [76] Z. Wang, X.-L. Qi, and S.-C. Zhang, *Phys. Rev. B* **84**, 014527 (2011).
- [77] T. Neupert, L. Santos, S. Ryu, C. Chamon, and C. Mudry, *Phys. Rev. B* **84**, 165107 (2011).
- [78] S. Ryu, J. E. Moore, and A. W. W. Ludwig, *Phys. Rev. B* **85**, 045104 (2012).
- [79] S. Ryu and S.-C. Zhang, *Phys. Rev. B* **85**, 245132 (2012).
- [80] X. Chen, Z.-C. Gu, Z.-X. Liu, and X.-G. Wen, *Phys. Rev. B* **87**, 155114 (2013).
- [81] Z.-C. Gu and X.-G. Wen, [arXiv:1201.2648](https://arxiv.org/abs/1201.2648).
- [82] X.-L. Qi, *New J. Phys.* **15**, 065002 (2013).
- [83] C. M. Ho and J. T. Chalker, *Phys. Rev. B* **54**, 8708 (1996).
- [84] A. W. W. Ludwig, M. P. A. Fisher, R. Shankar, and G. Grinstein, *Phys. Rev. B* **50**, 7526 (1994).